

Article

Effects of Surface Heterogeneity Due to Drip Irrigation on Scintillometer Estimates of Sensible, Latent Heat Fluxes and Evapotranspiration over Vineyards

Hatim M. E. Geli ^{1,*}, José González-Piqueras ², Christopher M. U. Neale ³, Claudio Balbontín ⁴ , Isidro Campos ² and Alfonso Calera ² 

¹ Department of Animal and Ranges Sciences, New Mexico Water Resources Research Institute, New Mexico State University, Las Cruces, NM 88003, USA

² Remote Sensing and GIS Group, Regional Research Institute, University of Castilla-La Mancha, Campus of Albacete, 13071 Ciudad Real, Spain; Jose.Gonzalez@uclm.es (J.G.-P.); campos.isidro@gmail.com (I.C.); Alfonso.Calera@uclm.es (A.C.)

³ Robert B. Daugherty Water for Food Global Institute, University of Nebraska-Lincoln, Lincoln, NE 68508, USA; cneale@nebraska.edu

⁴ Instituto de Investigaciones Agropecuarias, Centro de Investigación Intihuasi, Colina San Joaquín sn, La Serena Apartado Postal 36 B, Chile; claudio.balbontin@inia.cl

* Correspondence: hgeli@nmsu.edu; Tel.: +1-575-646-1640

Received: 1 December 2019; Accepted: 19 December 2019; Published: 24 December 2019



Abstract: Accurate estimates of sensible (H) and latent (LE) heat fluxes and actual evapotranspiration (ET) are required for monitoring vegetation growth and improved agricultural water management. A large aperture scintillometer (LAS) was used to provide these estimates with the objective of quantifying the effects of surface heterogeneity due to soil moisture and vegetation growth variability. The study was conducted over drip-irrigated vineyards located in a semi-arid region in Albacete, Spain during summer 2007. Surface heterogeneity was characterized by integrating eddy covariance (EC) observations of H, LE and ET; land surface temperature (LST) and normalized difference vegetation index (NDVI) data from Landsat and MODIS sensors; LST from an infrared thermometer (IRT); a data fusion model; and a two-source surface energy balance model. The EC observations showed 16% lack of closure during unstable atmospheric conditions and was corrected using the residual method. The comparison between the LAS and EC measurements of H, LE, and ET showed root mean square difference (RMSD) of 25 W m^{-2} , 19 W m^{-2} , and 0.41 mm day^{-1} , respectively. LAS overestimated H and underestimated both LE and ET by 24 W m^{-2} , 34 W m^{-2} , and 0.36 mm day^{-1} , respectively. The effects of soil moisture on LAS measurement of H was evaluated using the Bowen ratio, β . Discrepancies between H_{LAS} and H_{EC} were higher at $\beta \leq 0.5$ but improved at $1 \geq \beta > 0.5$ and $\beta > 1.0$ with R^2 of 0.76, 0.78, and 0.82, respectively. Variable vineyard growth affected LAS performance as its footprints saw lower NDVI_{LAS} compared to that of the EC (NDVI_{EC}) by ~ 0.022 . Surface heterogeneity increased during wetter periods, as characterized by the LST–NDVI space and temperature vegetation dryness index (TVDI). As TVDI increased (decreased) during drier (wetter) conditions, the discrepancies between H_{LAS} and H_{EC} , as well as LE_{LAS} and LE_{EC} decreased (increased). Thresholds of TVDI of 0.3, 0.25, and 0.5 were identified, above which better agreements between LAS and EC estimates of H, LE, and ET, respectively, were obtained. These findings highlight the effectiveness and ability of LAS in monitoring vegetation growth over heterogeneous areas with variable soil moisture, its potential use in supporting irrigation scheduling and agricultural water management over large regions.

Keywords: scintillometer; sensible and latent heat fluxes; evapotranspiration; NDVI–LST space and TVDI; surface energy balance; TSEB; soil moisture; drip-irrigated vineyards

1. Introduction

The increased pressure on water resources availability and use in arid and semi-arid regions has urged many agricultural water users to adopt water conservation practices, including drip irrigation [1–4]. In Spain and generally in the European Union (EU), drip irrigation is supported by many entities, strategies, and national plans, including the EU Water Framework Directive and National Irrigation Plan [3,5,6]. One of Spain's objectives of achieving water saving of 3000 Mm³/year has led to an exponential increase in drip-irrigated areas that exceeded 450% between 1989–2007, with another ~19% between 2007–2015 [3,7–9]. Currently, drip-irrigated areas account for ~49% of the total irrigated areas (1.79 Mha) that are mostly (~37%) covered with vineyards [3].

Vineyards have the ability to adapt to semi-arid environments and are of economic and social significance. Adoption of drip irrigation in vineyards can help in improving water management and in addressing imposed (controlled) water stress conditions. However, drip irrigation can introduce spatially variable soil moisture and vegetation growing conditions that add some challenges in obtaining accurate measurements of sensible (H), latent (LE) heat fluxes and actual evapotranspiration (ET).

Routine and accurate measurements of H, LE, and ET are required for an improved understanding of vegetation growth and water use. Eddy covariance (EC) and scintillometer systems are among the best methods that can provide such measurements, with both having pros and cons [10,11]. Some challenges can arise with the use of EC systems because they are relatively expensive, labor-intensive, requiring well-trained personnel, and provide local-scale observations [10,12]. Such local-scale observations do not adequately represent the spatial variability of the underlying surface. In many cases, large-scale observations over spatially heterogeneous surfaces are necessary. In these cases, a network of EC systems has been successfully used, which, however, adds some feasibility and management challenges.

Alternatively, advances in the scintillation method made it possible to address some of these challenges. Scintillometers can provide large-scale observations, require minimal data processing, and, technically, are relatively easy to maintain compared with a network of EC systems [13–15]. Scintillometers provide path-averaged measurements of H over distances of about 500 m up to 10 km. They can also provide area-averaged estimates of LE when combined with measurements of net radiation (Rn) and soil heat fluxes (G) [15–17]. Such large-scale observations are needed to provide more compatible observations for ground-truthing of remote sensing-based model estimates of H, LE, and ET [15,18]. Hence, scintillometers have advantages over EC systems in providing routine, efficient, and spatially representative large-scale observations that can enhance water managers' abilities to accurately monitor vegetation growth and water use [19].

Scintillometer observations are typically evaluated against those from EC systems. These evaluations often show a wide range of discrepancies depending on the underlying surface heterogeneity [14,15,17,20]. Some efforts have been made to identify the sources of these discrepancies, but there is still a need for additional evaluations. One of the main reasons for these discrepancies is attributed to differences in their represented spatial scales and surface heterogeneity.

The effects of some surface variables, including vegetation height, topography, and land cover types, on scintillometer applications were partially considered [14–16,21]. However, the effects of the most important variables—soil moisture and vegetation growth—have not been appropriately addressed [14,20,22]. These two variables play key roles in surface energy balance processes. Soil moisture affects partitioning of available energy (Rn – G) to H and LE. Vegetation growth affects surface roughness and ET. Some studies have accounted for surface variability due only to soil moisture, while the effects of vegetation growth on surface variability have been minimally considered or ignored. These two variables have unique combined effects in characterizing surface heterogeneity,

and hence, they need to be accounted for accordingly. For such, remote sensing can effectively and appropriately characterize surface heterogeneity.

A review of recent scintillometer applications suggested that remote sensing has been minimally utilized in addressing surface heterogeneity and its effects on scintillometry. For example, [20,22] used only land surface temperature (LST) over surface-irrigated olive trees and natural vegetation cover, respectively, to infer the effects of soil moisture variability on scintillometer-based estimates of H. On the other hand, vegetation growth has been extensively monitored using normalized difference vegetation index (NDVI) based on surface reflectance (i.e., optical remote sensing), as in [23–26]. However, the integration of surface variability, as characterized by using remote sensing-based indices such as NDVI to explain the performance of scintillometers, has been insufficiently studied.

The combined use of LST and NDVI can provide complimentary information about surface conditions [27]. Specifically, LST and NDVI can be graphically combined to form what is called LST–NDVI space that mostly takes the shape of a triangle diagram [27,28]. This empirical triangle concept was effectively used to describe and characterize the combined effects of soil moisture and vegetation growth over most surfaces [27,28]. In an LST–NDVI space, drier (wetter) surface conditions can be represented by lower (higher) NDVI, higher (lower) LST, and vice-versa that correspond to sparsely or stressed (dense or unstressed) vegetated surfaces. An LST–NDVI space can also be numerically represented in the form of a temperature vegetation dryness index (TVDI) that allows to quantitatively characterize soil water stress, ET, and surface and root zone soil moisture [27–29].

Generally, scintillometer behavior relative to irrigation events has been previously qualitatively evaluated, for example, in [16,20]. However, there is still a need to quantitatively characterize the combined effects of soil moisture and vegetation growth variability to appropriately evaluate surface heterogeneity due to irrigation practices (e.g., drip irrigation) and its effects on scintillometer measurements. To address this need, this study uniquely introduced the combined use of TVDI and scintillometry.

The goal of this study was to evaluate the effects of irrigation-induced surface heterogeneity in terms of soil moisture and vegetation growth variability on large aperture scintillometer (LAS) measurements of H, LE, and ET for efficient monitoring of crop water consumption and improved irrigation water management. To achieve this goal, this study uniquely integrated an EC system, thermal and optical remote sensing data, a data fusion model, and a surface energy balance model. The objectives of the study were to: Compare EC measurements with LAS estimates; use the spatial temporal adaptive reflectance fusion model (STARFM) to develop (i.e., fuse) a daily time series of NDVI based on Landsat and MODIS images; estimates of Rn, G, H, and LE using the two-source energy balance (TSEB) model; and characterize surface heterogeneity using LST–NDVI space and TVDI. The study highlights the performance of LAS during different soil moisture conditions by providing some explanations about when and why LAS and EC measurements can closely agree.

2. Data

2.1. Study Area

The experiment was carried out during the summer and fall of 2007 (1 August–31 October) in Central Spain (39°17' N, 1°59' W, 700 m above mean sea level—MSL) in the Albacete province, over drip-irrigated, row-oriented vineyards grown on vertical shoot positioned trellis [23]. H was measured simultaneously using an EC system and a LAS BLS900 (Scintec AG, Rottenburg, Germany). Other surface energy balance fluxes, including LE, Rn, and G, were also monitored throughout the growing season.

The study area was about 18.5 ha planted with four different 7-year-old varieties of grapes. The site was divided into 17 irrigation fields: The Cencibel variety was predominant, but Cabernet Sauvignon, Shiraz, and Merlot were also cultivated in smaller proportions. During the field campaign, other crops, including winter cereals and irrigated fruit trees, and a pine forest surrounded the

site (Figure 1). The vineyards were pruned during the dormant and growing seasons to adjust the vegetation development. No-tillage or cultivation was conducted during the growing season and the application of herbicides prevented the growth of weeds. The vine spacing was 1.5 m and the row spacing 3.0 m, which were oriented approximately in the north–south direction. The drip lines were placed on the trellis below the plants, with drippers spaced 1.0 m apart. Vineyard production in 2007 was $14,000 \text{ kg ha}^{-1}$, around 7 kg/tree , which was [23] similar to previous year yields, and no infection or diseases were detected in the plants during the growing season.

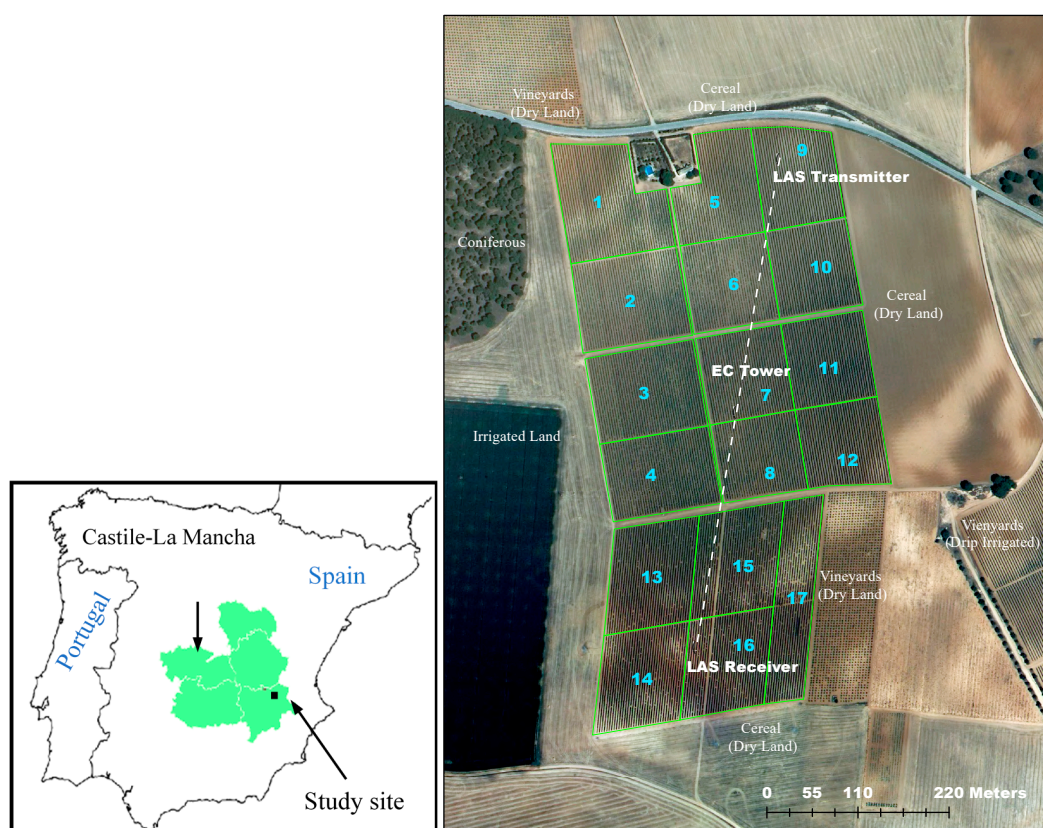


Figure 1. Aerial photograph of the study site with the 17 drip-irrigated vineyard fields, along with the location of the large aperture scintillometer (LAS) transmitter and receiver and eddy covariance (EC) tower. The numbers inside each polygon represent the field numbers. The LAS transmitter was located in Field 9 and the receiver was located in Field 16. The EC tower was located within Field 7 along the LAS path. The spaces between Fields 2 and 3, as well as other similar ones (~5–10 m), were for field accessibility purposes.

Irrigation was performed according to local practices, with a general rule of applying 22 mm of water to each field approximately every 12 days based on farmers' reports. However, observed irrigations over Field 7 showed that there is some variability in irrigation dates, with a total of 6 irrigations with 22 mm and a seventh one with about 11 mm, with an average of total applied irrigation depth of 143 mm throughout the growing season. The irrigation schedule over the other fields also showed similar variability (Appendix A—Figure A1). Unnecessary vegetation development increases crop water consumption, reduces soil water storage, and increases irrigation requirements. Therefore, the shoots were pruned in the experimental field around day of year (DOY) 187 and no new leaves or stems were observed after that date. So, the fractional vegetation cover (F_c) remained stable at 30%, as shown in Figure 2 [23]. The vegetation height at the beginning of the growing season was 70 cm and 164 cm by the end of the season, with an average width of foliage of 70 cm.

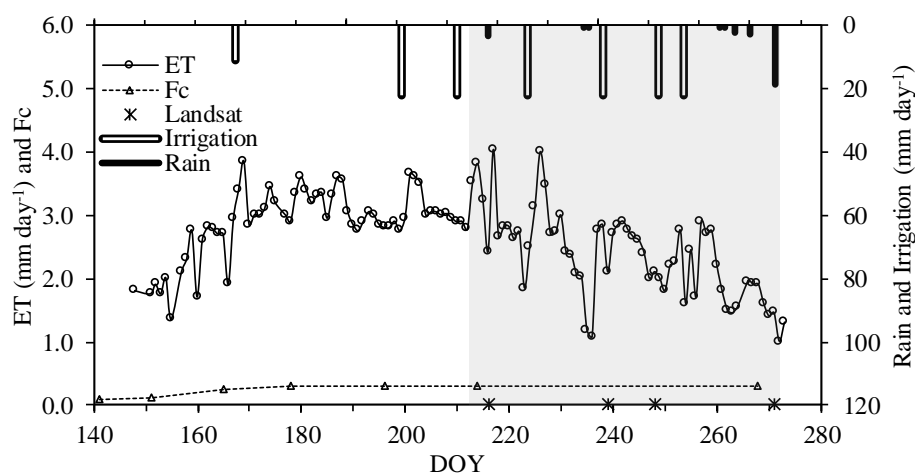


Figure 2. A plot of vineyards fraction of cover (Fc), actual evapotranspiration (ET) based on EC measurements, irrigation dates for Field 7, LAS measurements period, and Landsat overpass dates with respect to day of year (DOY) for year 2007.

2.2. LAS Measurements

The Boundary Layer Scintillometer BLS900 model from Scintec AG Rotternburg, Germany was used in this study. The LAS has an aperture diameter $D = 0.15$ and operates at a wavelength of 880 nm. Based on wind direction analysis, the LAS was deployed so that the wind passes dominantly perpendicular through its beam. The distance between the LAS transmitter and receiver was 640 m (Figure 1). The LAS path was relatively horizontal, as the transmitter and receiver were at 2.8 m and 3.5 m, respectively, above the ground. The measurement was sampled at 1 Hz and averaged over 1-min intervals. Air temperature (T_a) and atmospheric pressure (P) measurements were acquired using separate sensors that were integrated with the LAS system.

2.3. EC Measurements

The EC system was installed in the central part of the plot (Figure 1). The EC system consisted of a sonic anemometer CSAT-3 (Campbell Sci. Inst., Shepshed, Leicestershire LE12 9GX, UK), an infrared gas analyzer LI-7500 open system (LI-COR Inc., Lincoln, NE, USA) that records at 10 Hz (0.1 s), a humidity and temperature sensor HMP45C (Vaisala, Vantaa, Finland), and a datalogger CR5000, in which air density correction and some statistics were computed. The data were incorporated into high-frequency tables of fluxes every 30 min. The post-process was performed using the software TK2 [30], which mainly corrects the effects of separation between sensors, frequency attenuations by time averages, sensor length, and spurious values [23]. The sensors were located at 3 m above the ground-oriented northwest in the direction of prevailing winds (Figure 1).

R_n ($W m^{-2}$) was measured using a net radiometer CNR1 (Kipp & Zonen, Delft, The Netherlands), located 4.5 m above ground. The row orientation of the vineyards' trellis introduced sunlit and shading patterns that can affect G . To account for this effect, G ($W m^{-2}$) was measured at three positions spatially representative of the vineyard soil (i.e., the area covered by plants, at 0.75 m and 1.5 m from the plant row). G was calculated by correcting the heat fluxes measured by the flux plates by accounting for the effects of soil moisture content [31]. In each of the three G measurement positions, a Heat Flux Plate (HFP1) (Hukseflux, Delft, The Netherlands) was placed and buried at 8 cm deep along with two chrome–constantan thermocouples (TCAV, Type E) at 2 and 4 cm depths, together with a volumetric moisture reflectometer CS616 (Campbell Sci. Inst., Logan, UT, USA). A thermal infrared thermometer (IRT) was used to measure canopy and soil surface temperatures. A set of three Everest IRT (Everest Interscience Inc., Chino Hills, CA, USA) sensors accuracy of ± 0.3 °C. One IRT sensor was pointed at the vineyards to measure canopy temperature and the two other ones were pointed at sunlit and shaded

soils to provide an average soil surface temperature. This set of canopy and soil temperatures were used to estimate LST that was used to model surface energy balance fluxes, as described in Section 3.4.

Surface Energy Balance Lack of Closure

Lack of surface energy balance fluxes closure measured by EC systems is a known issue that yet remains unresolved [32], and it appears in terms of discrepancies between turbulent heat fluxes ($H + LE$) and available energy ($R_n - G$). The lack of closure in this study was evaluated using two well-known methods—the Bowen ratio (BR) and the Residual (Re) [32,33]. Generally, the BR method distributes the lack of closure between H and LE based on β (H/LE), and the Re method assumes this error is due to an underestimation in LE ($LE = R_n - G - H$) [32]. The two methods (i.e., BR and Re) were considered here because there is no consensus on a preferred one over the other. Lack of surface energy balance closure was addressed using daytime 8:30 a.m.–4:30 p.m. data during unstable atmospheric conditions.

2.4. Remote Sensing Data

2.4.1. Landsat Images

Four pairs of Landsat 5 images that consisted of LST and surface reflectance were used to characterize surface heterogeneity over the study site during the measurement period. Top of the atmosphere temperature images were atmospherically corrected to obtain at-surface LST using the radiative transfer model MODTRAN 4 [34]. These images were acquired during clear sky conditions on 4 and 27 August, and 5 and 28 September (Figure 2). Both datasets have a 30-m spatial resolution that allowed to account for field scale variability. Surface reflectance in near-infrared (NIR) and red bands were used to calculate NDVI as $(NIR - Red)/(NIR + Red)$.

Generally, over sparsely vegetated areas with dry soil surfaces, NDVI ranges between 0–1, with low and high values correspond to bare soils and full cover dense canopies, respectively. It can reach an asymptotic value of about 0.9 over most dense canopy covers. NDVI is not strongly sensitive and indirectly related to soil moisture in the root zone. It is directly related to and can be used to describe vegetation growth conditions and some plant biophysical properties over time. It provides a delayed response in terms of vegetation growth due to water stress [28]. A well-watered transpiring vegetation has higher NDVI values compared to water-stressed less transpiring one [27,35]. So, vineyard growth can be detected with NDVI spatially and temporally. On the other hand, LST is more sensitive to soil moisture and water-stressed conditions. As a biophysical response, a surface with well transpiring vegetation has lower LST compared to one with water-stressed conditions [27,29,35,36]. The Landsat data were used to develop the LST–NDVI space and TVDI.

2.4.2. MODIS Images

The study used a set of 56 images of MODIS NDVI for the period between 4 August and 28 September, 2007. MODIS data have a 250-m spatial resolution that does not allow to identify field scale surface heterogeneity. Therefore, the data were used in combination with those from Landsat 5 based on a data fusion approach to develop statistically representative Landsat-like NDVI images. This process allowed filling-in the gap between Landsat overpass dates using the spatial temporal adaptive reflectance fusion model (STARFM)—a data fusion approach developed by [37]. A brief description of STARFM is provided in Section 3.3. This NDVI time series helped in characterizing vineyards growth spatial variability over time.

2.5. Root Zone Soil Moisture Content

Soil moisture content measurements were acquired in Field 7 between two rows adjacent to the EC system at multiple layers below the surface at 10, 20, 30, 40, 50, and 80 cm using an EnviroScan soil water capacitance probe. Within the 3.0 m row spacing, two sets of probes were installed—adjacent to

the vine and near the emitters at each row. Another two sets of probes were installed at 75 cm away from each row and one set in the middle of the row (i.e., at 1.5 m from the row). The probes adjacent to, and those at 75 cm from, the vine showed a consistent soil moisture response with the irrigation events. The sensors that were located in the middle of the row, as well as those located at and below a depth of 50 cm, did not show any relevant response. The probes at shallow depths showed some response relative to significant rainfall events.

It should be noted that in this study, the probes were not calibrated to site-specific soil–water physical properties, including the range of available soil moisture between field capacity and wilting point. Measured soil hydrologic properties, including field capacity and permanent wilting point, were $0.29 \text{ cm}^3 \text{ cm}^{-3}$ and $0.14 \text{ cm}^3 \text{ cm}^{-3}$, respectively. Detailed soil properties were provided by [23], in which they conducted root zone water balance analysis to estimate ET. While the absolute accuracy of these measurements was not necessarily needed in this study, the evolution of soil moisture response to the irrigation events was certainly important and useful to explain the behavior of LAS and EC measurements of H and LE.

3. Methods

3.1. Estimates of H Using LAS

A scintillometer is a device that operates at a near-infrared electromagnetic wave to measure turbulent intensity fluctuations and present them in the form of a path-averaged structure parameter of the refraction index of air, C_n^2 . To this purpose, an electromagnetic radiation is transmitted over a (usually) horizontal path, and the corresponding intensity fluctuations are analyzed at the receiver. Both temperature and humidity fluctuations, C_T^2 and C_q^2 , respectively, give rise to C_n^2 . The relationship between C_T^2 and C_n^2 can be described by Equation (1) [13,38,39] as:

$$C_T^2 = C_n^2 \left(\frac{T_a^2}{\gamma \cdot P} \right)^2 \left(1 + \frac{0.03}{\beta} \right)^{-2} \quad (1)$$

where C_T^2 and C_n^2 are in $\text{K}^2 \text{ m}^{-2/3}$ and $\text{m}^{-2/3}$, respectively, P the atmospheric pressure (Pa), γ the refractive index coefficient for air ($0.78 \times 10^{-6} \text{ K Pa}^{-1}$), and T_a the air temperature ($^{\circ}\text{K}$). Equation (1) is a simplified version of Equation (A1) (Appendix B). In some cases, β can be obtained from the EC flux measurements. In this study, and to obtain LAS estimates of H (H_{LAS}) independent of β from EC measurements, β was estimated iteratively using available $(R_n - G)$ following the approach described by [16,40]. With the application of the Monin–Obukhov similarity theory (MOST), C_T^2 can be related to the temperature scale, T_* , by a universal function of stability parameter $\xi = (z_{\text{eff}} - d)/L$ as:

$$\frac{C_T^2 \cdot (z_{\text{eff}} - d)^{2/3}}{T_*^2} = f_T(\xi) \quad (2)$$

where z_{eff} is the LAS effective height (m) and L is the Monin–Obukhov length. For unstable conditions ($L < 0$) [40,41]:

$$f_T = 4.9 \left[1 - 6.1 \left(\frac{z_{\text{eff}} - d}{L} \right) \right]^{-2/3} \quad (3)$$

The effective height, z_{eff} , takes into account the effects of stability conditions and slanted paths as $z_{\text{eff}}^{-2/3} \cdot f_T(z_{\text{eff}}/L) = \int_{u=0}^{u=1} (1/z^{2/3}(u)) f_T(z(u)/L) G(u) du$ with $G(u)$ is the bell-shaped weighting function describing the contribution of C_n^2 to the total LAS signal at each point along the normalized path u [21], and $z(u)$ is the variable LAS beam height along the path (Figure 1). For slanted paths, $z(u)$ can be described relative to the maximum and minimum heights if the transmitter and/or the receiver z_{max}

and z_{min} , respectively, as $z(u) = z_{min}[1 + (z_{max}/(z_{min} - 1)) \cdot u]$. The Monin–Obukhov length, L , can be estimated as:

$$L = \frac{T_a \cdot u_*}{k \cdot g \cdot T_*} \quad (4)$$

with $k = 0.4$ is the von Karman constant, g the gravity ($9.81 \text{ m}\cdot\text{s}^{-2}$), and the friction velocity, u_* , can be estimated using the standard Businger–Dyer flux profile [42] as:

$$u_* = \frac{k \cdot U}{\ln\left(\frac{z_{eff} - d}{z_0}\right) - \psi_m\left(\frac{z_{eff} - d}{L}\right) + \psi_m\left(\frac{z_0}{L}\right)} \quad (5)$$

where U is the wind speed, ψ_m the stability correction function for the momentum transfer was calculated following [43,44] as $\psi_m = 2\ln[(1+x)/2] + \ln[(1+x^2)/2] - 2\arctan(x) + \pi/2$ with $x = [1 - 16(z_{eff} - d)/L]^{1/4}$, d is the displacement height, and z_0 is the roughness length. Both d and z_0 were calculated as a function of crop height h_c as $d = (2/3) \cdot h_c$ and $z_0 = (1/3) \cdot h_c$, respectively [45].

H_{LAS} can be estimated as:

$$H_{LAS} = \rho \cdot c_p \cdot u_* \cdot T_* \quad (6)$$

where ρ is the air density and c_p is the specific heat of air at constant pressure.

3.2. LST–NDVI Space, TVDI, and Spatial Heterogeneity

The LST–NDVI space can uniquely describe soil moisture variability and vegetation conditions over most surfaces [46]. As shown in Figure A2 (Appendix A), there is a negative correlation between LST and NDVI. In other words, as LST increases (decreases), NDVI decreases (increases). A plot of all pixel values of LST and NDVI for a given scene can reveal a triangle-shaped formulation with upper and lower bounds representing dry and wet edges, respectively. Partially vegetated surfaces fall in the space between these two edges. A set of isolines can be developed with varying slopes (Appendix A—Figure A2) that describe soil moisture variability, H, and LE [27,28,46]. In some cases, the LST–NDVI space is represented by a trapezoid to avoid some uncertainties that appear near the lower right angle of the triangle as the isolines are set very close to each other [29]. The LST–NDVI space has been used to qualitatively describe vegetation water stress and soil moisture variability [27,29,47,48].

Quantitatively, LST and NDVI can empirically be combined to TVDI that ranges between 0–1 for wettest to driest surfaces. The TVDI concept has been utilized to directly estimate surface and root zone soil moisture content [28,46,49]. In this study, the TVDI was used as an indicator of surface heterogeneity due to soil moisture, and to partially explain the corresponding behavior of LAS measurements. The TVDI can be estimated as:

$$TVDI = \frac{LST - LST_{min}}{LST_{max} - LST_{min}} \quad (7)$$

where LST_{min} is the minimum LST and LST_{max} the maximum LST that can be estimated as a function of NDVI as $LST_{max} = a + b \cdot NDVI$, where a and b are linear regression coefficients of the dry edge limit line. Based on the isolines, TVDI is simply the ratio between A to B (Appendix A—Figure A2). Two sets of TVDI were calculated, one was based on LST and NDVI from the four Landsat images. The second set was based on LST from the IRT and the NDVI from STARFM over Field 7. A consistent set of LST from the IRT and NDVI from STARFM was identified based on the time of the day that would correspond to Landsat typical overpass of 12:40 p.m. The TVDI was developed using LST–Ta to account for the effects of air temperature, as recommended by [28], and the corresponding dry edge line was developed following (Figure A1) [27,28,46].

3.3. Data Fusion

The STARFM is a data fusion approach that was developed to blend daily MODIS with the 16-day Landsat reflectance data. Using statistical methods, STARFM combines spectral similarities in Landsat and MODIS image pairs with temporal changes from the 250-m MODIS data to fill-in the gap between Landsat overpass dates to provide a consistent time series of Landsat-like data at 30-m spatial resolution. The STARFM has been used in many agricultural water management applications. It has been successfully applied with the TSEB model to provide field scale gap-filled time series of ET [50–53]. In this analysis, four pairs of Landsat and MODIS were used to develop statistically Landsat-like NDVI images from MODIS. This NDVI time series allowed to characterize vineyard growth variability within each field and within the LAS and EC footprints.

3.4. The TSEB Model

The thermal based two-source energy balance (TSEB) model [54,55] was used to provide independent estimates of H, LE, and $R_n - G$ to evaluate H_{LAS} . The TSEB model was applied using two different datasets—Landsat images and IRT point-based observations of LST. The TSEB model was chosen in this analysis due to its ability to provide accurate estimates of H and LE over a wide range of heterogeneous surfaces (e.g., row cropped fields) compared to other similar type of models. The TSEB model was successfully applied over heterogeneity surfaces similar to this site, including vineyard fields in California [35,50,56–58]. Based on a two-source concept, the TSEB model applies the surface energy balance equation over surface components (i.e., canopy and bare soil) separately and combines the fluxes at an air–canopy interface. The main assumption of the model is that LST can be decomposed based on the fraction of cover (f_c) [55] as:

$$T_R = [f_c \cdot T_c^4 + (1 - f_c) \cdot T_s^4]^{1/4} \quad (8)$$

with T_R is the LST or sometimes referred to as radiometric surface temperature, and T_c and T_s are canopy and bare soil temperatures (°K). The fraction of cover f_c viewed at nadir can be estimated as $f_c = 1 - e^{-(0.5 \cdot LAI)}$, where LAI is the leaf area index. A brief description of the TSEB model and its application over canopy and soil components is provided in Appendix C [54].

3.5. Footprint Model

The source areas (i.e., flux footprints) of the EC and LAS systems captured associated surface heterogeneity that contributed to measured fluxes. Flux footprints of each system partially integrated a number of fields or sub-fields (Figure 1). A footprint analysis was carried out to estimate these source areas for each system. The size and extent of a footprint depend on many factors, including measurement height, atmospheric stability, wind speed and direction, and aerodynamic roughness length. The EC system footprints were estimated using the footprint model by [59,60]. For the LAS footprints, [59,60] model was combined with a superposition approach, as described in [14,15,20]. More details about the footprint analysis are provided in Appendix D.

4. Results

4.1. Observed Surface Energy Balance Closure

Observed $H_{EC} + LE_{EC}$ showed a closure ratio (CR) of 84% of $R_n - G$ (Figure 3). In other words, an underestimation of 16% in available energy was either unmeasured or unexplained, with a root mean square difference (RMSD) and R^2 of 54 W m^{-2} and 0.69, respectively. Adjusted sensible heat flux using the BR method ($H_{EC \beta}$) showed a mean value of 111 W m^{-2} (standard deviation (SD) of 56 W m^{-2}), with a 15% increase compared to that of raw H_{EC} of 95 W m^{-2} (SD of 46 W m^{-2}). Similarly, adjusted latent heat flux using the Re ($LE_{EC Re}$) and BR ($LE_{EC \beta}$) methods resulted in mean values of

176 (SD of 89 W m⁻²) and 159 W m⁻² (SD of 78 W m⁻²), with about 30% and 15% increase, respectively, compared to that of LE_{EC} of 138 W m⁻² (SD of 68 W m⁻²).

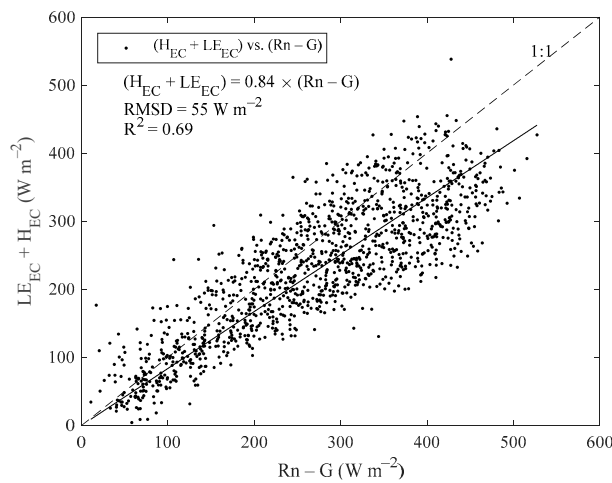


Figure 3. EC surface energy balance lack of closure based on a comparison between turbulence fluxes (LE + H) and available energy (Rn – G). RMSD, root mean square difference.

4.2. Comparison between H_{LAS} and H_{EC}

The mean and SD statistics of LAS and EC measurements of H, H_{LAS}, and H_{EC} and H_{EC β}, respectively, showed that the mean of H_{LAS} of 118 W m⁻² (SD of 52 W m⁻²) was ~26% higher than that of H_{EC} of 94 W m⁻² (SD of 56 W m⁻²) and 6% higher than that of H_{EC β} of 111 W m⁻² (SD of 46 W m⁻²). These statistics indicate that regardless of the method used to address lack of closure, H_{LAS} overestimated those obtained by the EC system. In other words, this result suggests that the flux footprint “seen” by the LAS experienced higher H with relatively drier surface conditions compared to that “seen” by the EC, as explained in more details in Section 5.

The comparison between H_{LAS} and H_{EC} showed some discrepancies, as indicated by an RMSD of 25 W m⁻² (R² of 0.77) with a narrow dispersion around the 1:1 line within a 95% confidence interval (Table 1 and Figure 4). A slightly lower agreement was observed between H_{LAS} and H_{EC β}, with an RMSD of 28 W m⁻² (R² of 0.72) and a wider dispersion around the 1:1 line. Also, the slope of the regression lines of 0.99 and 0.79 indicate a better agreement between H_{LAS} and H_{EC} compared to H_{LAS} and H_{EC β}, respectively. These comparisons indicate that the use of the Re method in this study to address lack of closure provided a better agreement compared to the BR method. Therefore, the analysis was completed using the Re method.

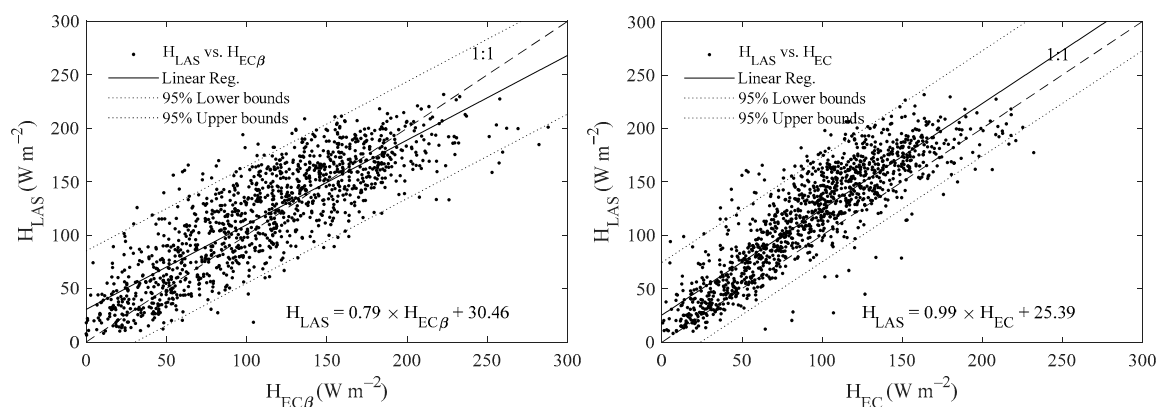


Figure 4. Comparisons between H_{LAS} and H_{EC β} (right), H_{LAS} and H_{EC Re} (left), along with corresponding linear regression and 95% confidence intervals.

Table 1. Summary of sensible heat flux comparison and regression statistic.

Equation	Slope a	Intercept b (W m ⁻²)	RMSD (W m ⁻²)	R ²	MBD* (W m ⁻²)	No. Data Points
$H_{LAS} = a \cdot H_{EC} + b$	0.99	25	25	0.77	24	1244
$H_{LAS} = a \cdot H_{EC} \beta + b$	0.79	31	28	0.72	7	1244

* Mean bias difference (MBD).

4.3. H_{LAS} , Soil Moisture, and Vegetation Spatial Variability

4.3.1. H_{LAS} and β

The effects of soil moisture temporal variability on H_{LAS} were evaluated using β . Generally, higher soil moisture content can lead to an increase in LE (and ET), decrease in H, and, consequently, lower β values [35]. In this study, β values were divided into three categories, including $\beta \leq 0.5$, $1 \geq \beta > 0.5$, and $\beta > 1$. The first two categories generally indicate that LE (and ET) > H. The third β category indicates that H > LE. A comparison between H_{LAS} and H_{EC} for each β category is shown in Figure 5. The data in the third β category suggest that the site experienced relatively drier conditions compared to the other two categories. At $\beta \leq 0.5$, H_{LAS} overestimated H_{EC} by a mean bias difference (MBD) of 34 W m⁻². At $1 \geq \beta > 0.5$, the MBD decreased to 27 W m⁻², and at $\beta > 1$, H_{LAS} underestimated H_{EC} by an MBD of -14 W m⁻². In other words, as β increased (i.e., drier surface conditions became dominant), the agreement between H_{LAS} and H_{EC} improved as the MBD consistently decreased. Also, R² of 0.76, 0.78, and 0.82 for $\beta \leq 0.5$, $1 \geq \beta > 0.5$, and $\beta > 1$, respectively, show consistently improved agreement between H_{LAS} and H_{EC} as β increased.

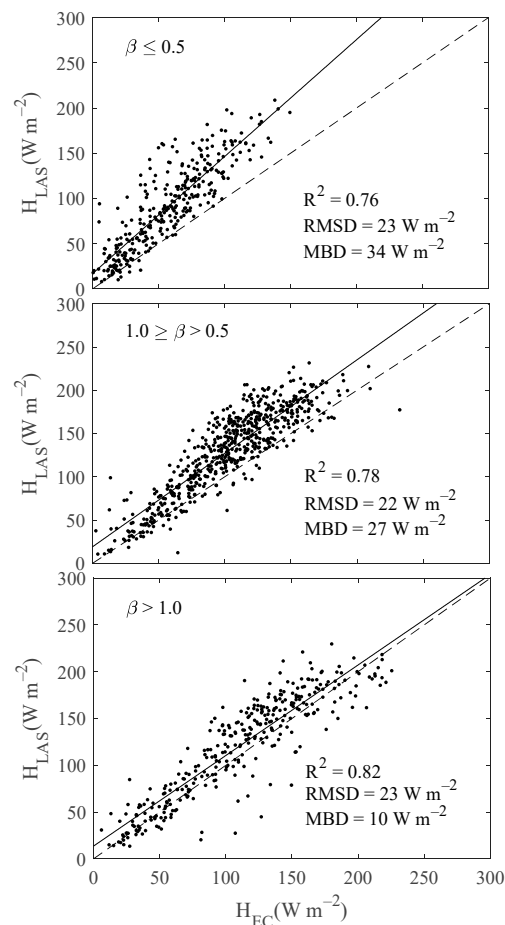


Figure 5. Comparison between H_{LAS} and H_{EC} at different β categories, with of $\beta \leq 0.5$ (top), $1.0 \geq \beta > 0.5$ (middle), and $\beta > 1.0$ (bottom).

4.3.2. LST-NDVI Space and Spatial Heterogeneity

This section first shows an evaluation of LST, NDVI, and an LST-NDVI space based on the four Landsat images. Second, the LST-NDVI space was then used to develop a TVDI relationship based on the Landsat data. Third, a TVDI time series was developed based on a relatively longer dataset of LST from the IRT and NDVI from STARFM. Fourth, the TVDI time series was used as a surrogate for soil moisture to evaluate the H_{LAS} and LE_{LAS} .

NDVI Variability

The average NDVI over each field for all four Landsat images was calculated and is shown in Figure 6. The NDVI indicates that each field experienced relatively variable growing conditions. For example, the average NDVI of all dates over Fields 2, 6, and 9 consistently show lower NDVI of 0.32, 0.30, and 0.31, compared to those over Fields 7 and 8 of 0.36 and 0.39, respectively. The corresponding average NDVI that represented, or “as seen” by, the LAS and EC footprints is shown on the x-axis in Figure 6 as points 18 and 19, and referred to herein as $NDVI_{LAS}$ and $NDVI_{EC}$, respectively. The NDVI that represented (or as seen by) the EC system was estimated by overlying (superimposing) the EC footprints over the NDVI images. Using the footprint values (which are in dimensionless units), a weighted sum of NDVI values within the footprint boundaries was calculated to estimate $NDVI_{EC}$ for each image data and time. A similar process regarding the calculation of $NDVI_{LAS}$ was followed. The results show that both $NDVI_{LAS}$ and $NDVI_{EC}$ of 0.35 and 0.37, respectively, were relatively higher than those of over Fields 2, 6, and 9. This pair of four NDVI values shows that $NDVI_{LAS}$ was consistently, but slightly, lower than $NDVI_{EC}$ (Figure 6).

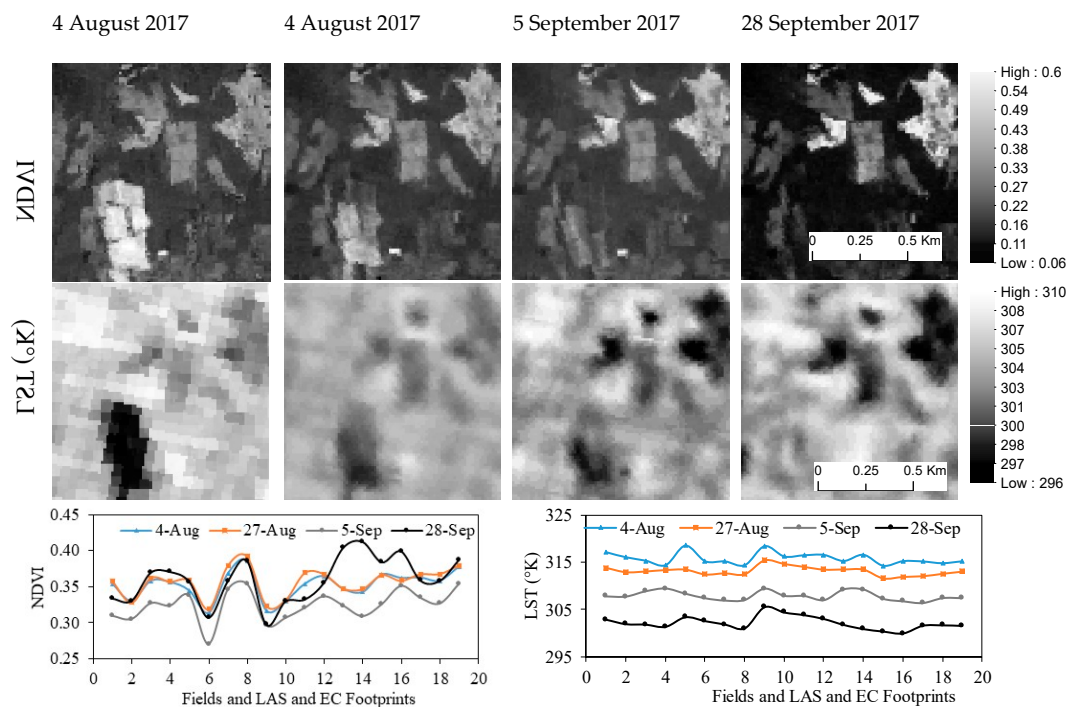


Figure 6. Normalized difference vegetation index (NDVI) (top row) and land surface temperature (LST) (middle row) based on Landsat Images along with plots of a spatial distribution of NDVI (bottom left) and LST (bottom right) of all fields.

A time series of footprint-integrated pairs of $NDVI_{LAS}$ and $NDVI_{EC}$ was developed using the STARFM-based NDVI maps (Figure 7). Images with cloudy sky conditions were excluded (11 images out of 54). The results show that $NDVI_{LAS}$ and $NDVI_{EC}$ were closely correlated ($R^2 = 0.90$), and the average $NDVI_{LAS}$ was ~ 0.022 lower than $NDVI_{EC}$.

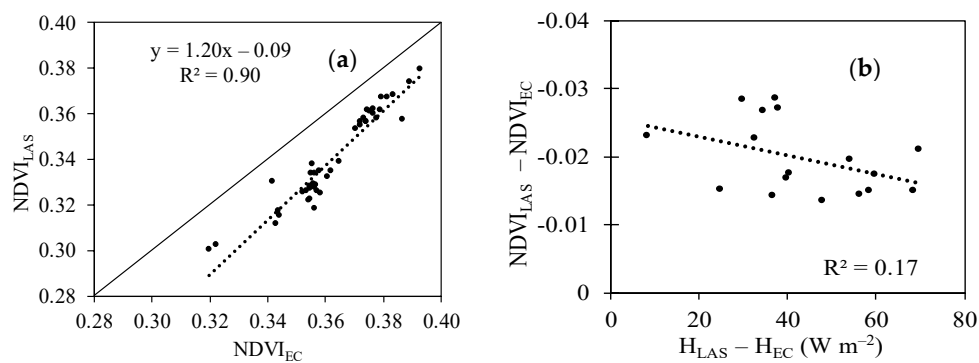


Figure 7. Scatter plots of (a) $NDVI_{LAS}$ and $NDVI_{EC}$, and (b) $NDVI_{LAS} - NDVI_{EC}$ compared to $H_{LAS} - H_{EC}$.

LST–NDVI Space

Using the triangle concept (Figure A2), regression lines (or isolines) were developed to represent the data for each of the four Landsat image dates (Figure 8). The negative slope shown by all regression lines indicates that during each day, as LST increased, NDVI decreased. The standard deviation of NDVI (σ_{NDVI}) for each day (or isoline) varied from low to high, from 0.019, 0.020, 0.021, and 0.033 from the upper- to the lower-most isoline, respectively. The σ_{NDVI} suggests that there was a relatively larger spatial vineyard growth variability during wetter conditions (i.e., lower-most isoline) compared to drier ones. The mean LST (μ_{LST}) varied from high to low from the upper- to the lower-most isoline from 315.9, 313.2, 307.9, and 302.2 °K, respectively. The μ_{LST} also indicates that the surface exhibited higher LST (i.e., warmer) during drier conditions compared to wetter ones (i.e., cooler). This qualitative evaluation of LST–NDVI space was necessary to develop a TVDI time series based on the IRT data.

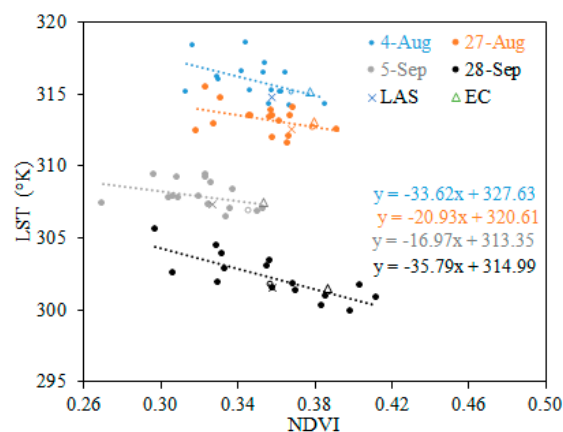


Figure 8. Plot of LST–NDVI space, along with isolines for each Landsat overpass date.

4.3.3. H_{LAS} and TVDI

Estimates of TVDI

As an initial evaluation, the obtained TVDI, which ranged from 0–1, was plotted against H_{EC} (not shown) to make sure that it followed the known behavior, as described by [27,28,46,49]. A positive correlation between TVDI and H_{EC} was obtained. The lowest average TVDI (about 0.20) was on 28 September and corresponded to the lowest average LST (~302.2 °K). The observed behavior of the TVDI in this study agreed with the fact that higher TVDI corresponds to drier conditions [28,46,49], higher LST – T_a [29], and higher H [28,29].

Estimates of H_{TSEB}

The TSEB model was used to estimate H_{TSEB} and $(Rn - G)_{TSEB}$ that can be used to evaluate both $H_{LAS} - H_{EC}$ and $H_{LAS} - H_{TSEB}$ against TVDI and to calculate LE_{LAS} , respectively. The TSEB model was applied using two LST datasets from the Landsat images and the IRT. Estimates of H based on the Landsat data (or remote sensing) ($H_{TSEB RS}$) and those based on the IRT ($H_{TSEB IRT}$) are shown in Figure 9. Two different comparisons were conducted— H_{EC} against $H_{TSEB IRT}$ and H_{LAS} against $H_{TSEB IRT}$. The comparison between H_{EC} and $H_{TSEB IRT}$ showed an RMSD and R^2 of 35 W m^{-2} and 0.71, respectively, with a narrow scatter distribution around the 1:1 line. Slightly lower agreement was obtained between H_{LAS} and $H_{TSEB IRT}$, with an RMSD and R^2 of 51 W m^{-2} and 0.64, respectively. One of the main reasons for the increased discrepancies between H_{LAS} and $H_{TSEB IRT}$ was attributed to differences in the spatial representation of $H_{TSEB IRT}$ (at a point) to that of H_{LAS} . Estimates of $H_{TSEB RS}$ did not have enough data points that could be meaningfully evaluated. However, a visual inspection of Figure 9 showed that the footprint-integrated H_{EC} and H_{LAS} were closely correlated with $H_{TSEB RS}$. Overall, these TSEB model results are consistent with previous studies [14,35,50,56,61,62] and allowed the use of $H_{TSEB IRT}$ to characterize surface conditions.

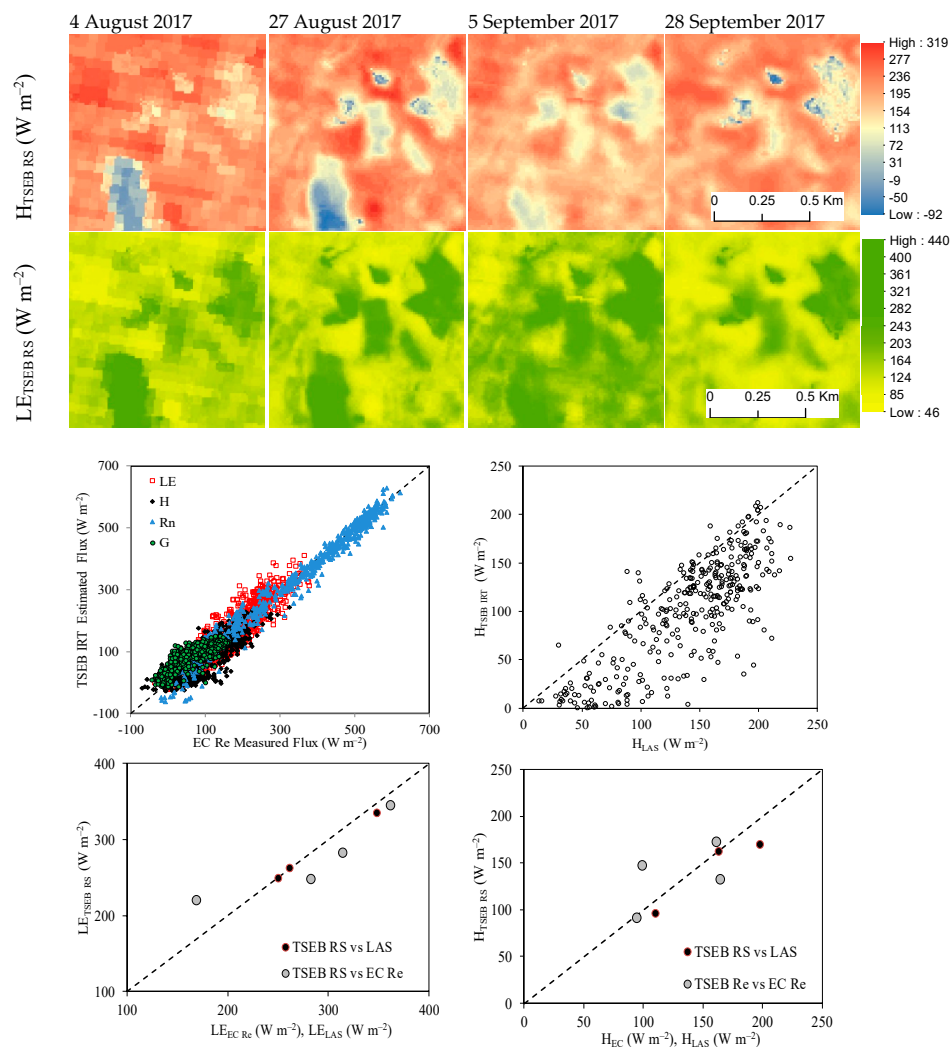


Figure 9. Maps of the two-source energy balance (TSEB) model estimates of H_{TSEB} (top row) and LE_{TSEB} (second row) based on Landsat, comparison between EC Re measurements and TSEB IRT estimates of Rn, G, H, and LE (third row left), scatter plot of H_{LAS} and $H_{TSEB IRT}$ (third row right), comparison of footprint integrated $LE_{TSEB RS}$, $LE_{EC Re}$, and LE_{LAS} (bottom left), comparison of $H_{TSEB RS}$, H_{EC} , and H_{LAS} (bottom right).

H_{LAS} and TVDI

Estimates of H_{LAS} , H_{EC} , and $H_{TSEB\ IRT}$ can be considered independent of each other—a condition that allowed to adequately evaluate soil moisture and vegetation growth variability, as characterized by the TVDI. The comparisons between $H_{LAS} - H_{EC}$ and $H_{LAS} - H_{TSEB\ IRT}$ against TVDI are shown in Figure 10. The results show a negative correlation ($R^2 = 0.55$) between $H_{LAS} - H_{EC}$ and TVDI, which indicates that as the discrepancies between H_{LAS} and H_{EC} decreased, the TVDI increased. A relatively higher correlation ($R^2 = 0.66$) was obtained between $H_{LAS} - H_{TSEB\ IRT}$ and TVDI based on a smaller sample size. This comparison also provides a similar indication of decreased discrepancies between H_{LAS} and $H_{TSEB\ IRT}$ with increased TVDI. In other words, both comparisons indicate that the agreement between H_{LAS} and both H_{EC} and $H_{TSEB\ IRT}$ improved during higher TVDI or specifically drier surface conditions. This consistent behavior of H_{LAS} and TVDI suggests that TVDI can effectively be used to evaluate the effects of surface heterogeneity due to irrigation on LAS performance.

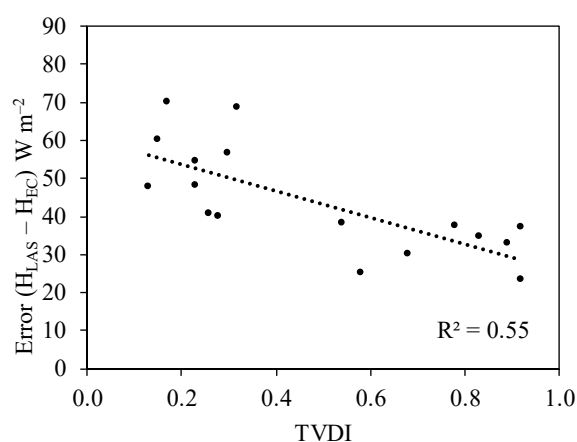


Figure 10. Comparison between the error in H ($H_{LAS} - H_{EC}$) and temperature vegetation dryness index (TVDI).

4.4. Estimates of LE and ET

4.4.1. Estimates of LE_{LAS}

LE_{LAS} was estimated as the residual of the energy balance equation as $LE_{LAS} = R_n - G - H_{LAS}$. Estimates of $(R_n - G)_{TSEB\ IRT}$ based on the TSEB and IRT data (Section 3.4) were used to obtain relatively independent LE_{LAS} compared to $LE_{EC\ Re}$. Estimates of $(R_n - G)_{TSEB\ IRT}$ resulted in an RMSD and R^2 of $34\ W\ m^{-2}$ and 0.93, respectively, with an underestimation indicated by an MBD of $-30\ W\ m^{-2}$ when compared with $(R_n - G)_{EC}$ (Figure 11). Two different estimates of LE_{LAS} were obtained: $LE_{LAS\ TSEB\ IRT}$ based on $(R_n - G)_{TSEB\ IRT}$ and $LE_{LAS\ EC}$ based on $(R_n - G)_{EC}$. $LE_{LAS\ TSEB\ IRT}$ and $LE_{LAS\ EC}$ were evaluated against $LE_{EC\ Re}$ and $LE_{TSEB\ IRT}$, respectively (Figure 11). These comparisons show that both estimates of $LE_{LAS\ TSEB\ IRT}$ and $LE_{LAS\ EC}$ consistently underestimated $LE_{EC\ Re}$ and $LE_{TSEB\ IRT}$, respectively. The comparison between $LE_{LAS\ EC}$ and $LE_{TSEB\ IRT}$ showed a reasonable distribution around the 1:1 line, with an RMSD and R^2 of $39\ W\ m^{-2}$ and 0.71, respectively, and underestimation indicated by an MBD of $-20\ W\ m^{-2}$. The comparison between $LE_{LAS\ TSEB\ IRT}$ and $LE_{EC\ Re}$ showed a narrower distribution around the 1:1 line, with an RMSD and R^2 of $30\ W\ m^{-2}$ and 0.82, respectively, and underestimation indicated by an MBD of $-59\ W\ m^{-2}$ (Figure 11).

4.4.2. LE_{LAS} and TVDI

The differences $LE_{LAS\ TSEB\ IRT} - LE_{EC\ Re}$ and $LE_{LAS\ EC} - LE_{TSEB\ IRT}$ were compared with TVDI to evaluate the effects of soil moisture and vegetation growth variability on LE_{LAS} . The obtained results show that both differences were negatively correlated with TVDI with first comparison (i.e., $LE_{LAS\ TSEB\ IRT} - LE_{EC\ Re}$ versus TVDI) resulted in $R^2 = 0.72$, and the second one (i.e., $LE_{LAS\ EC} -$

LE_{TSEB IRT} versus TVDI) indicated an $R^2 = 0.57$. These negative correlations suggest that as the two differences increased, the TVDI decreased (as soil moisture increased). These comparisons were based on a much smaller sample sizes due to the need of using consistent datasets of LE_{LAS TSEB IRT}, LE_{EC Re}, LE_{LAS EC}, and LE_{TSEB IRT}. Therefore, they were used to qualitatively evaluate LE_{LAS} and TVDI behavior. LE_{LAS EC} was used to provide a quantitative evaluation of TVDI, as discussed in Section 5.7.

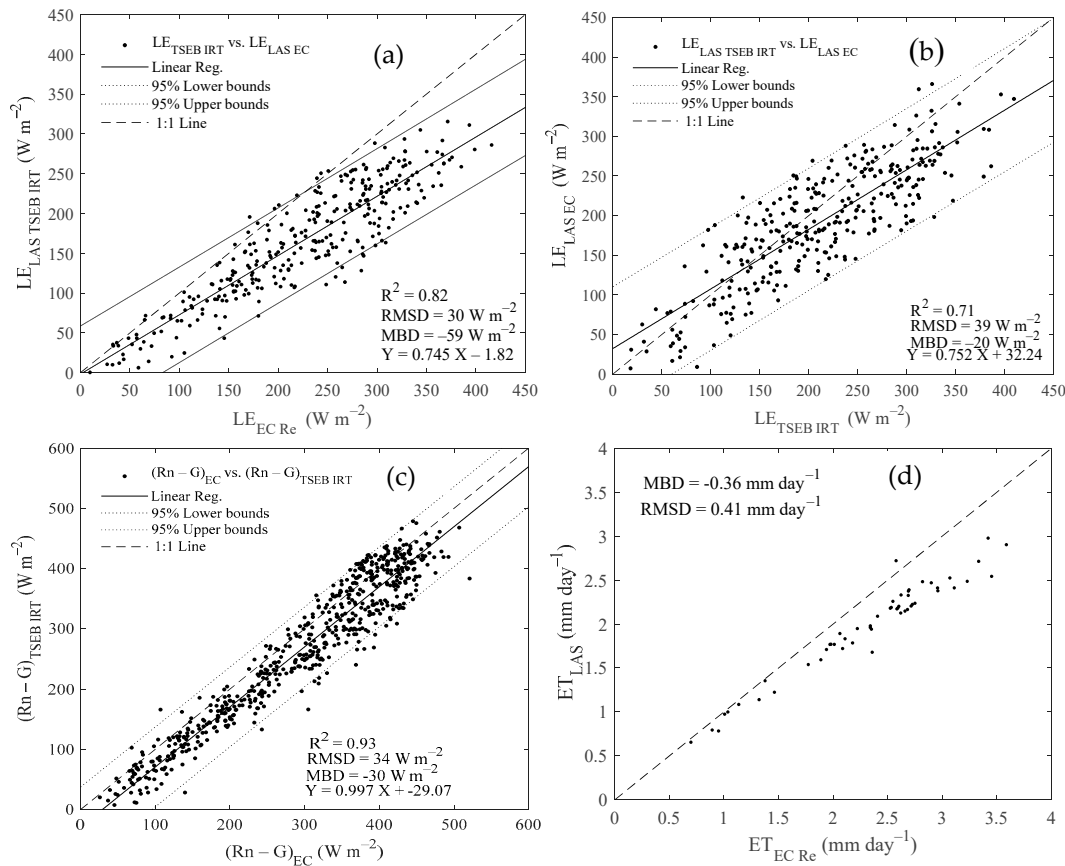


Figure 11. Comparisons between (a) LE_{LAS TSEB IRT} and LE_{EC Re}, (b) LE_{LAS EC} and LE_{TSEB IRT}, (c) (Rn - G)_{TSEB IRT} versus (Rn - G)_{EC}, and (d) ET_{LAS} and ET_{EC Re}.

4.4.3. Estimates of ET

Estimates of ET_{LAS} and ET_{EC Re} based on LE_{LAS} and LE_{EC Re}, respectively (Figure 11), show a good agreement, with an RMSD of 0.41 mm day⁻¹. An underestimation of ET_{LAS} to ET_{EC Re} was noticed with an MBD of -0.36 mm day⁻¹. This result was consistent with that obtained in Section 4.3, which indicated an overestimation of H_{LAS} to H_{EC} and, consequently, an underestimation of LE_{LAS} to LE_{EC Re}. The obtained mean values for ET_{LAS} and ET_{EC Re} were 2.1 and 2.5 mm day⁻¹, respectively. A better LAS performance was visually observed at ET_{LAS} ≤ 2 mm day⁻¹ with increased discrepancies above this value.

5. Discussion

5.1. Lack of Closure

Observed lack of closure of EC measurements was within the typical acceptable range of 15–20% over agricultural areas [12,32,40,56]. Closure ratios (CRs) of 0.84 and 0.86 were reported over heterogeneous vineyards in California [56] and homogeneous rainfed soybean in Iowa [63–65]. Also, the lack of closure in this study had minimal effects on the discrepancies between H_{LAS} and H_{EC}. Generally, lack of closure is partly attributed to mismatch in spatial scale of measurements

(i.e., $R_n - G$ versus $H + LE$) and the underlying surface heterogeneity [12,32,65,66]. As indicated by [22], a combination of $CR \leq 0.80$ and surface heterogeneity can increase these discrepancies. This combination highlighted the need to evaluate the effects of surface heterogeneity on LAS in this study.

5.2. H_{LAS} and H_{EC}

The obtained RMSD between H_{LAS} and H_{EC} was within acceptable levels of accuracy. Reported typical levels of accuracy of H measurements for LAS and EC were within 30 W m^{-2} [40] and 50 W m^{-2} [12,67,68], respectively. Also, [20] indicated that acceptable differences between H_{LAS} and H_{EC} were within 50 W m^{-2} . [20] compared H_{LAS} against H_{EC} over flood-irrigated olive orchards and obtained an RMSD of 36, 29, and 63 W m^{-2} before, after, and during irrigation events, respectively, assuming heterogeneous soil moisture during irrigation and homogeneous otherwise. Also, [16] obtained an RMSD of 63 W m^{-2} over drip-irrigated orange orchards.

Previous studies evaluated LAS performance mainly relative to three factors: Vegetation cover uniformity, placement of EC and LAS considering their footprints, and soil moisture effects on surface heterogeneity [16,20,22,69]. In this study, the first two factors had relatively minimal effects compared to the latter. The site had homogenous cover dominantly vegetated with one vineyard variety with a constant h_c and F_c during the measurement period [23]. A footprint analysis showed that the EC footprints lied mostly within Field 7 (and Field 3), and that of the LAS partially integrated nine fields, including Fields 2, 3, 4, 5, 6, 7, 8, 13, and 15. Field 7 accounted for 27% of the LAS footprints (Figure 12). The EC footprints accounted for ~20% of, and most importantly lied entirely within, that of the LAS—such setup is considered the most ideal placement of LAS and EC systems to obtain comparable measurements [22,69]. Thus, this evaluation suggests that surface heterogeneity due to soil moisture and vegetation growth (i.e., vigor and greenness) variability can mainly explain the discrepancies between H_{LAS} of H_{EC} .

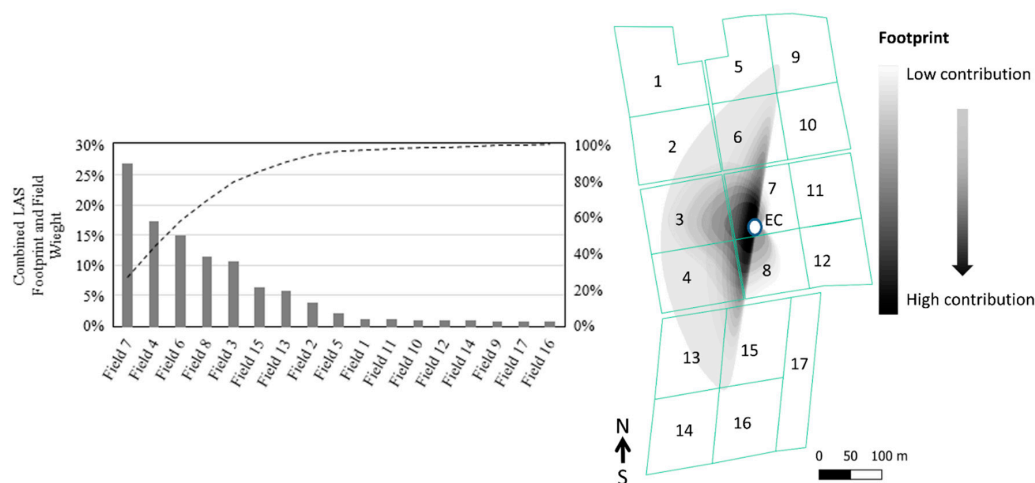


Figure 12. The vineyard fields and the dominant LAS and EC footprints (left), and the weighted contribution of the vineyard fields on LAS and EC observations (right).

5.3. H_{LAS} and β

Considering soil moisture effects, the use of β in Equation (1) can also partly explain some of the discrepancies between H_{LAS} and H_{EC} based on the humidity correction factor and the corresponding assumptions. The humidity correction factor $[(1 + 0.03/\beta)^{-2}]$ partly affects the accuracy of C_T^2 and H_{LAS} [38,39]. The humidity correction factor is less than 10% for $\beta \geq 0.6$ [21]. Thus, it has minimal effects on H_{LAS} accuracy at larger β and no need to use it at $\beta > 1$ [14,21,40]. On the other hand, the uncertainty in H_{LAS} can reach up to 15% and 48% at $\beta = 0.3$ and $\beta < 0.3$, respectively [40]. In other

words, decreased uncertainty in H_{LAS} during drier conditions (i.e., $H > LE$ and $\beta > 1$) can lead to improved agreement with H_{EC} compared to periods with increased soil moisture ($H < LE$ and $\beta < 1$).

Moreover, regardless of the correction factor, its assumptions can still lead to increased discrepancies during wet conditions. The obtained results indicated that even when accounting for this factor, the discrepancies between H_{LAS} and H_{EC} at $\beta \leq 0.5$ increased. Equation (1) is a simplified form of Equation (A1) (Appendix B) that relates C_n^2 , C_T^2 , and C_q^2 [39], assuming that the correlation between T and q, $R_{tq} = +1$. This assumption removes the direct dependency of C_n^2 on C_q^2 , and hence reduces its contribution to $[(1 + 0.03/\beta)^{-2}]$. Many studies argued the applicability of this assumption over a wide range of moisture conditions. In some cases, $R_{tq} < 1$, especially during periods with increased soil moisture content [20,38,70]. [20] found that $R_{tq} \leq 0.75$, during which R_{wt} and R_{wq} did not follow each other, resulting in ~4% overestimation by H_{LAS} over flood-irrigated olive orchards. Unfortunately, in this study, there were no data to evaluate the R_{tq} , but the study by [20] was used as a guidance, as they indicated that $R_{tq} \approx 0.6$ for $\beta \leq 0.5$.

The violation of this assumption, which led to overestimation of H_{LAS} to H_{EC} , is typical during transitions from dry to wet periods, and largest during low H values that occur during nearly neutral unstable conditions (i.e., low β values), as indicated by [71]. During such periods, the near surface layer (i.e., internal adapted layer) is not fully developed compared to very unstable conditions (i.e., during high β values). In this study, a better agreement between H_{LAS} and H_{EC} was clearly obtained during drier conditions (i.e., at $\beta > 1$) and a reasonable one was obtained at $1 \geq \beta > 0.5$. These results are consistent with previous findings by [20,40,70,71]

5.4. NDVI Variability

The NDVI provided a good indication of how healthy and variable the vineyards were growing spatially and temporally. All vineyard fields showed a consistent NDVI spatial variability over time. Such consistent NDVI behavior over time was indicative of soil temporal variability. NDVI spatial variability indicated that each vineyard field experienced physiologically variable growth compared to other fields. Spatially variable soil properties can partly explain this variable growth, since all fields were dominantly planted with one variety and there was no reported water or nutrient stress conditions. The soils in the study site were classified as Inceptisol with a sand, clay, gravel texture [23]. These types of soils are known for their variable productivity, including texture and water-holding capacity. A similar behavior was observed over vineyards grown in California, US in fields with variable soil physical properties that caused variable growing conditions and lower yields [56].

Based on NDVI, the vineyards within the EC footprints showed relatively better growth compared to that within the LAS. This can partially explain the overestimation of H_{LAS} to H_{EC} and it is also consistent with the basic concepts of near surface flux exchange [55,72,73]. An evaluation of $NDVI_{LAS} - NDVI_{EC}$ against $H_{LAS} - H_{EC}$ showed that $H_{LAS} - H_{EC}$ slightly increased as $NDVI_{LAS} - NDVI_{EC}$ decreased (Figure 7b) with a low correlation ($R^2 = 0.17$). This low correlation was partly because the study was conducted during vineyard full cover period with relatively constant F_c and minimal variation in NDVI (Figure 2). A more effective approach in these cases is to monitor vineyards throughout the growing season. $NDVI_{LAS} - NDVI_{EC}$ decreased as $H_{LAS} - H_{EC}$ increased during relatively wet periods (increased moisture content). The typical acceptable error between H_{LAS} and H_{EC} of $\sim 50 \text{ W m}^{-2}$ [20,40] corresponded to $NDVI_{LAS} - NDVI_{EC}$ of ~ 0.018 . The average of $NDVI_{LAS} - NDVI_{EC}$ of 0.022 can partly explain the overestimation of H_{LAS} to H_{EC} of MBE of 24 W m^{-2} (Table 1).

5.5. LST–NDVI Space and Soil Moisture

The LST–NDVI space offered an elaborate characterization of surface heterogeneity, as it combines soil moisture and vegetation growth variability based on LST and NDVI, respectively. The results indicated that during any day, some fields experienced higher LST (i.e., drier conditions) and lower NDVI compared to others. Lower σ_{NDVI} during drier conditions suggested relatively more spatial variability (i.e., relatively heterogeneous) compared to higher σ_{NDVI} during wetter conditions (i.e.,

relatively homogeneous). Also, higher μ_{LST} consistently corresponded with higher σ_{NDVI} during drier conditions. The μ_{LST} for each isoline (or day) was used to explain and identify the status of the soil moisture of the root zone. The upper- and lower-most isolines can represent the driest and wettest edges of the triangle [27,28,46,49]. The μ_{LST} was compared with a normalized soil moisture content in Field 7 to evaluate its temporal variability. A normalized soil moisture (NSM) content was calculated as $NSM = [(SM - SM_{min}) / (SM_{max} - SM_{min})]$, where SM is the half-hour volumetric soil moisture content, and SM_{max} and SM_{min} are the maximum and minimum soil moisture contents. The soil moisture status was the lowest at the upper-most isoline during 4 August (16%), followed by 27 August (56%), 5 September (60%), and 28 September (70%) (Figure A3). The 4 August was about four days before irrigation, 27 August was three days after irrigation, and 5 and 28 September were just one to two days after irrigation (Figure A3).

This elaborate characterization can provide a more effective and practical approach to address some challenges in monitoring LAS performance over heterogeneous areas. Some studies characterized homogenous surface conditions based on before and after irrigation events, during which H_{LAS} and H_{EC} closely agreed compared to during irrigation [20,74]. However, over large areas, challenges can arise in identifying such periods due to lack of irrigation, reporting or subjectively identifying periods before and after irrigation which can lead to misleading indications. This qualitative evaluation highlighted the advantage of using the LST–NDVI space to account for soil moisture and vegetation growth variability and its appropriateness to evaluate H_{LAS} . A quantitative evaluation of H_{LAS} based on LST–NDVI space and TVDI can further provide a more effective approach.

5.6. H_{LAS} and TVDI

The obtained results are consistent with the empirical triangle concept, as they showed increased TVDI that coincided with higher H during drier surface conditions (i.e., lower surface and root zone soil moisture content) [27–29,49,75–78]. Also, improved agreement between H_{LAS} and H_{EC} was obtained during higher TVDI during relatively drier conditions. These results suggested that $H_{LAS} - H_{EC}$ increased during relatively wet periods as TVDI decreased (i.e., higher soil moisture contents and LE). To provide a more effective way to evaluate H_{LAS} , a TVDI threshold of 0.30 was identified, above which $H_{LAS} - H_{EC}$ fell within an acceptable level of accuracy of 50 W m^{-2} .

Figure 10 provides significantly useful information for practical applications. For example, thresholds of TVDI can be developed and combined with the large-scale estimates of H_{LAS} and LE_{LAS} to manage irrigation more accurately. This analysis indicated that regardless of knowing the irrigation schedule, the TVDI was able to appropriately characterize surface conditions and LAS performance during varying soil moisture content compared to using LST or NDVI individually, as used in previous studies [20,22,74]. While these results are promising, it was important to note that adding more LST images and soil moisture measurements can provide more spatially representative TVDI.

5.7. Estimates of LE_{LAS} and ET

The results indicated that $(Rn - G)_{TSEB\ IRT}$ consistently underestimated $(Rn - G)_{EC}$. This can partly be attributed to spatial scale mismatch between the IRT and EC systems' footprints of 2–3 m point-based and a few hundred meters, respectively. Consequently, these discrepancies affected $LE_{LAS\ TSEB\ IRT}$, $LE_{LAS\ EC}$, and the agreement between LAS and EC estimates. An improved agreement between LE_{LAS} and LE_{EC} can be obtained when using $(Rn - G)_{EC}$ compared to using $(Rn - G)$ independent from EC measurements, as indicated by some previous studies. For example, $(Rn - G)_{IRT}$ data were used to estimate LE_{LAS} over flood-irrigated winter wheat, olive yard, and drip-irrigated orange orchards that resulted in an RMSD of 49, 56, and 62 (with R^2 of 0.74, 0.71, and 0.68), respectively, when compared with LE_{EC} [16]. In another study by Hoedjes et al. [79], $(Rn - G)_{EC}$ data were used simultaneously to address lack of energy balance closure and calculate LE_{LAS} over wheat, and resulted in an R^2 of 0.97 when compared with LE_{EC} . However, using $(Rn - G)_{EC}$ in this manner does not provide fully independent LE_{LAS} and LE_{EC} . Though, such use was not uncommon, especially in cases

with data limitations [79]. Also, previous inter-comparison studies of independent measurements of $R_n - G$ showed increased correlation ($R^2 > 0.95$), with discrepancies mainly attributed to instrumentation error [80,81]. By following this approach in this study, an improved agreement between $LE_{LAS\ EC}$ and $LE_{EC\ Re}$ was obtained with RMSD, R^2 , and MBD of $19\ W\ m^{-2}$, 0.93, and $-34\ W\ m^{-2}$, respectively.

On the other hand, it was also noticed that the discrepancies in both comparisons (i.e., $LE_{LAS\ TSEB\ IRT}$ vs. $LE_{EC\ Re}$ and $LE_{LAS\ EC}$ vs. $LE_{TSEB\ IRT}$) decreased (increased) as LE decreased (increased) during drier (wetter) conditions. The correlation between $LE_{LAS\ TSEB\ IRT} - LE_{EC\ Re}$ and TVDI, as well as $LE_{LAS\ EC} - LE_{TSEB\ IRT}$ and TVDI, suggested that both $LE_{LAS\ TSEB\ IRT} - LE_{EC\ Re}$ and $LE_{LAS\ EC} - LE_{TSEB\ IRT}$ increased during relatively higher soil moisture conditions, as characterized by decreased TVDI and increased LE [27,28,46,49]. This behavior of LE_{LAS} versus TVDI is consistent with the obtained results (Section 4.3) when comparing H_{LAS} discrepancies with TVDI.

The observed TVDI behavior in response to soil moisture variation suggested its ability to provide practical means to evaluate LE_{LAS} and to manage irrigation over large areas. In this study, periods with relatively higher LE occurred within ~5 days after significant wetting events (i.e., irrigation or rain). This number of days varied from one field to another, and hence, its use was challenging, not practical, and subjective. For such, the TVDI was compared with $LE_{LAS\ EC} - LE_{EC}$ to develop a threshold to evaluate LE_{LAS} performance. The datasets of $LE_{LAS\ TSEB\ IRT} - LE_{EC\ Re}$ and $LE_{LAS\ EC} - LE_{TSEB\ IRT}$ were not considered in this case because of the limited data points. A threshold of TVDI = 0.25 was identified, above which a higher agreement between LE_{LAS} and $LE_{EC\ Re}$ was obtained, which can vary with the use of a larger dataset.

Measured $ET_{EC\ Re}$ values throughout the growing season were $\leq 4\ mm\ day^{-1}$ with $\leq 2\ mm\ day^{-1}$ observed during periods with low soil moisture content or near the end of the season (Figure 2). Smaller discrepancies between ET_{LAS} and $ET_{EC\ Re}$ appeared during these periods and increased right after irrigation or significant rain events when ET_{EC} was around or $> 3\ mm\ day^{-1}$. In other words, during relatively drier conditions, the LAS and EC systems showed better agreement in ET estimates.

The difference between ET_{LAS} and $ET_{EC\ Re}$ estimates was within 16%, which is within reported levels of accuracies. The study by [82] compared ET_{LAS} with those from a remote sensing-based model called SEBAL over a mixed vegetation cover and obtained an error of 17%. Other studies compared ET_{EC} with TSEB model estimates and reported an RMSD within $0.6\ mm\ day^{-1}$ over agricultural sites with similar heterogeneity to this study [35,50,56]. On the other hand, suggested acceptable accuracies of ET measurements from LAS and EC were mostly within 10–15%, but in some cases, can reach up to 30% [10,11]. The difference $ET_{LAS} - ET_{EC\ Re}$ increased as TVDI decreased during wet conditions. A TVDI threshold of ~0.5 was identified, below which $ET_{LAS} - ET_{EC\ Re}$ exceeded 15%. Additional analysis with larger dataset will need to be conducted in the future to further support this finding.

6. Conclusions

This study evaluated the effects of surface heterogeneity on LAS performance due to soil moisture and vegetation growth variability caused by irrigation practices. LAS observations and estimates of H, LE, and ET were obtained over row drip-irrigated vineyards during 1 August–31 October 2007 in Albacete, Spain. The study used a suite of methods that included EC observations of H, LE, and ET; LST and NDVI from Landsat and MODIS sensors; additional LST from an IRT; a data fusion model to develop a time series of NDVI; and a surface energy balance model to estimate H and LE. The EC observations showed a lack of closure of 16% during unstable atmospheric conditions and was corrected using the Residual method. Good agreements were obtained between LAS and EC estimates of H, LE, and ET with an RMSD of $25\ W\ m^{-2}$, $19\ W\ m^{-2}$, $0.41\ mm\ day^{-1}$, respectively. LAS overestimated H and underestimated both LE and ET by $24\ W\ m^{-2}$, $34\ W\ m^{-2}$, and $0.36\ mm\ day^{-1}$, respectively.

The effects of soil moisture on H_{LAS} was evaluated using the Bowen ratio, β . Higher discrepancies between H_{LAS} and H_{EC} were obtained at $\beta \leq 0.5$, but improved agreement was shown at $1 \geq \beta > 0.5$

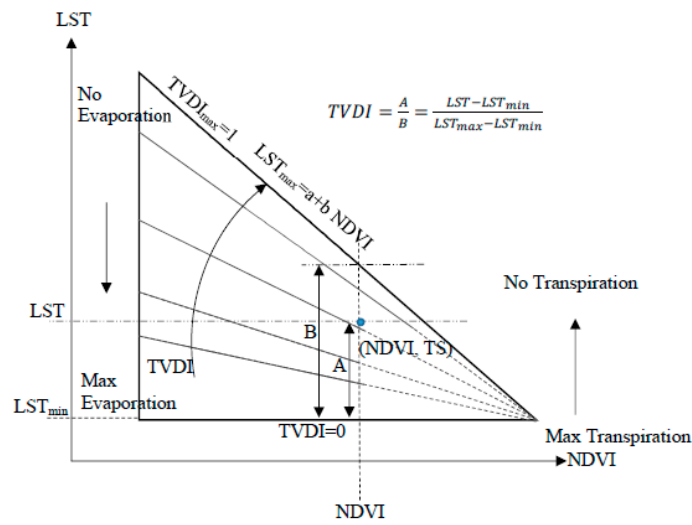


Figure A2. A description of the LST-NDVI space and TVDI calculations.

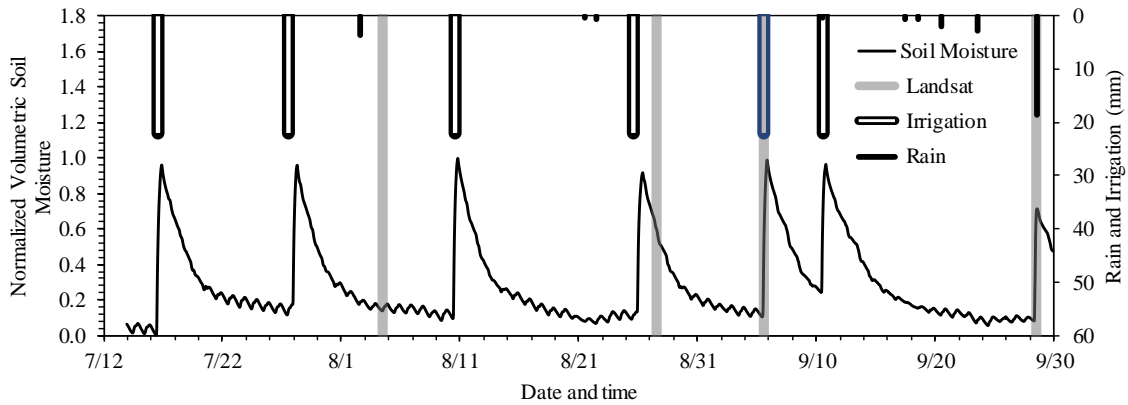


Figure A3. A description of relative soil moisture content, rain, and irrigation time series Field 7, along with Landsat overpass dates.

Appendix B

Appendix B.1. Estimation of C_T^2 as a Function of C_n^2

Based on [38,39], C_T^2 is related to C_n^2 as follows:

$$C_n^2 \approx \frac{A_T^2}{T^2} C_T^2 \left(1 + \frac{A_q}{q} \frac{\bar{T}}{A_T} \frac{c_p}{L_v} \beta^{-1} \right)^2 \quad (A1)$$

where A_T and A_q are coefficients that can be calculated as a function of atmospheric pressure (p), air temperature (T), humidity (q), and optical wavelength as $A_T = -0.78 \cdot (p/T) \times 10^{-6}$ and $A_q = -57.22 \cdot q \times 10^{-6}$, c_p is the specific heat at constant pressure. [38] found that during certain conditions, the factor in front of β^{-1} (i.e., $\left(\frac{A_q}{q} \frac{\bar{T}}{A_T} \frac{c_p}{L_v}\right)$) equals 0.031 and Equation (A1) is simplified to Equation (1), as shown in Section 3.1 above.

Appendix C

Appendix C.1. TSEB Model Description

The surface energy balance equations over canopy and bare soil components can be described as:

$$R_n = H + LE + G \quad (\text{A2})$$

$$R_{nc} = H_c + LE_c + G \quad (\text{A3})$$

$$R_{ns} = H_s + LE_s + G \quad (\text{A4})$$

where subscripts *s* and *c* refer to soil and canopy components. The sensible heat flux can be estimated as:

$$H_c = \rho c_p \frac{T_c - T_{ac}}{r_x} \quad (\text{A5})$$

$$H_s = \rho c_p \frac{T_s - T_{ac}}{r_s} \quad (\text{A6})$$

$$H = H_c + H_s = \rho c_p \frac{T_{ac} - T_a}{r_a} \quad (\text{A7})$$

where T_{ac} is the air temperature at an air–canopy interface, ρ the air density taken as $1.24 \text{ (kg m}^{-3}\text{)}$, c_p the specific heat of air taken as $1005 \text{ (J kg}^{-1} \text{K}^{-1}\text{)}$, r_x the total boundary layer resistance of the complete canopy leaves, r_s the resistance to heat flow in the boundary layer immediately above the soil surface, and r_a is the aerodynamic resistance to heat transfer. The latent heat flux for each component can be estimated as:

$$LE_s = R_{ns} - G - H_s \quad (\text{A8})$$

$$LE_c = \alpha_{PT} f_g \frac{\Delta}{\Delta + \gamma} R_{nc} \quad (\text{A9})$$

where G can be estimated as 0.30 of R_{ns} , α_{PT} is the Priestly–Taylor constant taken as 1.26, f_g the fraction of leaf area index (*LAI*) that is green, Δ the slope of the saturation vapor pressure versus temperature curve, and γ the psychrometric constant. The initial value of $\alpha_{PT} = 1.26$ is used for well-water unstressed vegetation, which can further be adjusted by following an iterative process to account for stressed vegetation. More details about the TSEB model and the methods followed to estimate the different variables can be found in many applications [35,50,56,62].

Appendix D

Appendix D.1. Footprint Analysis

The footprint function f represents the contribution per unit surface flux of each unit element in the upwind surface area to a measured vertical flux. This function relates the vertical flux, $F(x, y, z_m)$, measured at height z_m to the spatial distribution of surface emission fluxes $F(x', y', z = 0)$:

$$F(x, y, z_m) = \int_{-\infty}^{+\infty} \int_{-\infty}^x F(x', y', z = 0) f(x - x', y - y', z_m) dx' dy' \quad (\text{A10})$$

where x and y are the upwind and crosswind distances (m), respectively, from the point of measurements. The model assumes that the turbulent flux field is horizontally homogeneous, and therefore the footprint depends only on the separation between the measurement point and the site of the elemental emission

flux. The separation in the wind direction is $(x-x')$ and that in the crosswind direction is $(y-y')$. In this analysis, the three-dimensional footprint function for scalar fluxes was calculated as:

$$F_P(x, y, z_m) = \frac{f^{-y}(x, z_m)}{\sigma_y \sqrt{2\pi}} \exp\left[-\frac{1}{2}\left(\frac{y}{\sigma_y}\right)^2\right] \quad (\text{A11})$$

where σ_y is the standard deviation of the lateral spread which can be estimated as a function of the plume travel time x/U and the standard deviation of the lateral wind fluctuations σ_v as $\sigma_y = \sigma_v \frac{x}{U}$ with U is the advection speed. The footprint function can be calculated as:

$$f^{-y}(x, z_m) = \frac{d\bar{z}}{dx} \frac{z_m}{\bar{z}^2} \frac{\bar{U}(z_m)}{\bar{U}(c\bar{z})} A \cdot \exp\left[-\left(\frac{z_m}{b\bar{z}}\right)^r\right] \quad (\text{A12})$$

where \bar{z} is the mean plume height for diffusion from a surface source (m), z_m is the measurement height, $\bar{u}(z)$ is the mean wind profile variables A , b and c are functions of the gamma function (Γ), and r is the Gaussian plume model shape parameter. The diffusion in the lateral direction is assumed Gaussian [59].

To obtain the three-dimensional footprint function for the LAS, Equation (A12) was combined with the spatial weighting function of the scintillometer [14,15,20]. The LAS path was thought to consist of a series of single observation points, which, for each a single source area, was calculated using Equation (A11). Each of these source areas was then multiplied by the LAS weighting function, $G(u)$. The summation of all individual points was normalized by the total of the source areas, which then yielded the LAS weighted footprint.

References

1. Black, M. *The Atlas of Water: Mapping the World's Most Critical Resource*, 3rd ed.; University of California Press: Oakland, CA, USA, 2016.
2. Jiménez, B. *Managing Water Resources in Arid and Semi Arid Regions of Latin America and Caribbean (MWAR—LAC): Accomplishment Report*; International Hydrological Programme UNESCO: Paris, France, 2016.
3. Sese-Minguez, S.; Boesveld, H.; Asins-Velis, S.; Van der Kooij, S.; Maroulis, J. Transformations accompanying a shift from surface to drip irrigation in the Canyoles Watershed, Valencia, Spain. *Water Altern.* **2017**, *10*, 81–99.
4. Ortega-Reig, M.; Sanchis-Ibor, C.; Palau-Salvador, G.; García-Mollá, M.; Avellá-Reus, L. Institutional and management implications of drip irrigation introduction in collective irrigation systems in Spain. *Agric. Water Manag.* **2017**, *187*, 164–172. [[CrossRef](#)]
5. Martínez-Aldaya, M.; Llamas, M.R. *Water Footprint Analysis (Hydrologic and Economic) of the Guadiana River Basin*; Value of Water Research Report 35, No. 3; Unesco-IHE Institute for Water Education: Delft, The Netherlands, 2009.
6. Todo, K.; Sato, K. Directive 2000/60/EC of the European Parliament and of the Council of 23 October 2000 establishing a framework for Community action in the field of water policy. *Environ. Res. Q.* **2002**, 66–106.
7. Lecina, S.; Isidoro, D.; Playan, E.; Aragües, R. Irrigation modernization and water conservation in Spain: The case of Riegos del Alto Aragón. *Agric. Water Manag.* **2010**, *97*, 1663–1675. [[CrossRef](#)]
8. Gómez-Limón, J.A.; Picazo-Tadeo, A.J. Irrigated agriculture in Spain: Diagnosis and prescriptions for improved governance. *Int. J. Water Resour. D* **2012**, *28*, 57–72. [[CrossRef](#)]
9. Lopez-Gunn, E.; Zorrilla, P.; Prieto, F.; Llamas, M.R. Lost in translation? Water efficiency in Spanish agriculture. *Agric. Water Manag.* **2012**, *108*, 83–95. [[CrossRef](#)]
10. Allen, R.G.; Pereira, L.S.; Howell, T.A.; Jensen, M.E. Evapotranspiration information reporting: I. Factors governing measurement accuracy. *Agric. Water Manag.* **2011**, *98*, 899–920. [[CrossRef](#)]
11. Kleissl, J.; Gomez, J.; Hong, S.H.; Hendrickx, J.M.H.; Rahn, T.; Defoor, W.L. Large aperture scintillometer intercomparison study. *Bound. Layer Meteorol.* **2008**, *128*, 133–150. [[CrossRef](#)]
12. Alfieri, J.G.; Blanken, P.D. How representative is a point? The spatial variability of flux measurements across short distances. *Remote Sens. Hydrol.* **2012**, 210–214.

13. De Bruin, H.A.R.; Van den Hurk, B.J.J.M.; Kohsiek, W. The scintillation method tested over a dry vineyard area. *Bound. Layer Meteorol.* **1995**, *76*, 25–40. [[CrossRef](#)]
14. Geli, H.M.E.; Neale, C.M.U.; Watts, D.; Osterberg, J.; De Bruin, H.A.R.; Kohsiek, W.; Pack, R.T.; Hipps, L.E. Scintillometer-based estimates of sensible heat flux using lidar-derived surface roughness. *J. Hydrometeorol.* **2012**, *13*, 1317–1331. [[CrossRef](#)]
15. Meijninger, W.M.L.; Hartogensis, O.K.; Kohsiek, W.; Hoedjes, J.C.B.; Zuurbier, R.M.; De Bruin, H.A.R. Determination of Area-Averaged Sensible Heat Fluxes with a Large Aperture Scintillometer over a Heterogeneous Surface - Flevoland Field Experiment. *Bound. Layer Meteorol.* **2002**, *105*, 37–62. [[CrossRef](#)]
16. Ezzahar, J.; Chehbouni, A.; Er-Raki, S.; Hanich, L. Combining large aperture scintillometer and estimates of available energy to derive evapotranspiration over several agricultural fields in a semi-arid region. *Plant Biosyst.* **2009**, *143*, 209–221. [[CrossRef](#)]
17. Ezzahar, J.; Chehbouni, A.; Hoedjes, J.; Ramier, D.; Boulain, N.; Boubkraoui, S.; Cappelaere, B.; Descroix, L.; Mougnot, B.; Timouk, F. Combining scintillometer measurements and an aggregation scheme to estimate area-averaged latent heat flux during the AMMA experiment. *J. Hydrol.* **2009**, *375*, 217–226. [[CrossRef](#)]
18. Watts, C.J.; Chehbouni, A.; Rodríguez, J.C.; Kerr, Y.H.; Hartogensis, O.K.; De Bruin, H.A.R. Comparison of sensible heat flux estimates using AVHRR with scintillometer measurements over semi-arid grassland in northwest Mexico. *Agric. For. Meteorol.* **2000**, *105*, 81–89. [[CrossRef](#)]
19. Moorhead, J.E.; Marek, G.W.; Colaizzi, P.D.; Gowda, P.H.; Evett, S.R.; Brauer, D.K.; Marek, T.H.; Porter, D.O. Evaluation of Sensible Heat Flux and Evapotranspiration Estimates Using a Surface Layer Scintillometer and a Large Weighing Lysimeter. *Sensors* **2017**, *17*, 2350. [[CrossRef](#)]
20. Hoedjes, J.C.B.; Chehbouni, A.; Ezzahar, J.; Escadafal, R.; De Bruin, H.A.R. Comparison of Large Aperture Scintillometer and Eddy Covariance Measurements: Can Thermal Infrared Data Be Used to Capture Footprint-Induced Differences? *J. Hydrometeorol.* **2007**, *8*, 194–206. [[CrossRef](#)]
21. Hartogensis, O.K.; Watts, C.J.; Rodríguez, J.C.; De Bruin, H.A.R. Derivation of an effective height for scintillometers: La Poza experiment in Northwest Mexico. *J. Hydrometeorol.* **2003**, *4*, 915–928. [[CrossRef](#)]
22. Liu, S.M.; Xu, Z.W.; Wang, W.; Jia, Z.Z.; Zhu, M.J.; Bai, J.; Wang, J.M. A comparison of eddy-covariance and large aperture scintillometer measurements with respect to the energy balance closure problem. *Hydrol. Earth Syst. Sci.* **2011**, *15*, 1291–1306. [[CrossRef](#)]
23. Campos, I.; Neale, C.M.U.; Calera, A.; Balbontán, C.; González-Piqueras, J. Assessing satellite-based basal crop coefficients for irrigated grapes (*Vitis vinifera* L.). *Agric. Water Manag.* **2010**, *98*, 45–54. [[CrossRef](#)]
24. Jones, H.G.; Vaughan, R.A. *Remote Sensing of Vegetation: Principles, Techniques, and Applications*; Oxford University Press: Oxford, UK, 2010.
25. Enciso, J.; Avila, C.A.; Jung, J.; Elsayed-Farag, S.; Chang, A.; Yeom, J.; Landivar, J.; Maeda, M.; Chavez, J.C. Validation of agronomic UAV and field measurements for tomato varieties. *Comput. Electron. Agric.* **2019**, *158*, 278–283. [[CrossRef](#)]
26. Hunsaker, D.J.; Barnes, E.M.; Clarke, T.R.; Fitzgerald, G.J.; Pinter, P.J., Jr. Cotton irrigation scheduling using remotely sensed and FAO-56 basal crop coefficients. *Trans. ASAE* **2005**, *48*, 1395–1407. [[CrossRef](#)]
27. Sandholt, I.; Rasmussen, K.; Andersen, J. A simple interpretation of the surface temperature/vegetation index space for assessment of surface moisture status. *Remote Sens. Environ.* **2002**, *79*, 213–224. [[CrossRef](#)]
28. Garcia, M.; Fernandez, N.; Villagarcia, L.; Domingo, F.; Puigdefaábregas, J.; Sandholt, I. Accuracy of the Temperature-Vegetation Dryness Index using MODIS under water-limited vs. energy-limited evapotranspiration conditions. *Remote Sens. Environ.* **2014**, *149*, 100–117. [[CrossRef](#)]
29. Moran, M.S.; Clarke, T.R.; Inoue, Y.; Vidal, A. Estimating Crop Water-Deficit Using the Relation between Surface-Air Temperature and Spectral Vegetation Index. *Remote Sens. Environ.* **1994**, *49*, 246–263. [[CrossRef](#)]
30. Mauder, M.; Foken, T.; Clement, R.; Elbers, J.A.; Eugster, W.; Grünwald, T.; Heusinkveld, B.; Kolbe, O. Quality control of CarboEurope flux data. Part 2: Inter-comparison of eddy-covariance software. *Biogeosciences* **2008**, *5*, 451–462. [[CrossRef](#)]
31. Payero, J.O.; Neale, C.M.U.; Wright, J.L. Estimating Soil Heat Flux for Alfalfa and Clipped Tall Fescue Grass. *Appl. Eng. Agric.* **2005**, *21*, 1–9. [[CrossRef](#)]
32. Twine, T.E.; Kustas, W.P.; Norman, J.M.; Cook, D.R.; Houser, P.R.; Meyers, T.P.; Prueger, J.H.; Starks, P.J.; Weseley, M.L. Correcting eddy-covariance flux underestimates over a grassland. *Agric. For. Meteorol.* **2000**, *103*, 279–300. [[CrossRef](#)]

33. Balbontin-Nesvara, C.; Calera-Belmonte, A.; Gonzalez-Piqueras, J.; Campos-Rodriguez, I.; Lopez-Gonzalez, M.L.; Torres-Prieto, E. Vineyard Evapotranspiration Measurements in a Semiarid Environment: Eddy Covariance and Bowen Ratio Comparison. *Agrociencia* **2011**, *45*, 87–103.
34. Berk, A.; Bernstein, L.S.; Anderson, G.P.; Acharya, P.K.; Robertson, D.C.; Chetwynd, J.H.; Adler-Golden, S.M. MODTRAN cloud and multiple scattering upgrades with application to AVIRIS. *Remote Sens. Environ.* **1998**, *65*, 367–375. [[CrossRef](#)]
35. Neale, C.M.U.; Geli, H.M.E.; Kustas, W.P.; Alfieri, J.G.; Gowda, P.H.; Evett, S.R.; Prueger, J.H.; Hipps, L.E.; Dulaney, W.P.; Chavez, J.L.; et al. Soil water content estimation using a remote sensing based hybrid evapotranspiration modeling approach. *Adv. Water Resour.* **2012**, *50*, 152–161. [[CrossRef](#)]
36. Goetz, S.J. Multi-sensor analysis of NDVI, surface temperature and biophysical variables at a mixed grassland site. *Int. J. Remote Sens.* **1997**, *18*, 71–94. [[CrossRef](#)]
37. Gao, F.; Masek, J.; Schwaller, M.; Hall, F. On the blending of the Landsat and MODIS surface reflectance: Predicting daily Landsat surface reflectance. *IEEE Trans. Geosci. Remote Sens.* **2006**, *44*, 2207–2218.
38. Moene, A.F. Effects of water vapour on the structure parameter of the refractive index for near-infrared radiation. *Bound. Layer Meteorol.* **2003**, *107*, 635–653. [[CrossRef](#)]
39. Wesely, M.L. Combined Effect of Temperature and Humidity Fluctuations on Refractive-Index. *J. Appl. Meteorol.* **1976**, *15*, 43–49. [[CrossRef](#)]
40. Solignac, P.A.; Brut, A.; Selves, J.L.; Béteille, J.P.; Gastellu-Etchegorry, J.P.; Keravec, P.; Béziat, P.; Ceschia, E. Uncertainty analysis of computational methods for deriving sensible heat flux values from scintillometer measurements. *Atmos. Meas. Tech.* **2009**, *2*, 741–753. [[CrossRef](#)]
41. Andreas, E.L. Estimating Cn^2 over Snow and Sea Ice from Meteorological Data. *J. Opt. Soc. Am. A* **1988**, *5*, 481–495. [[CrossRef](#)]
42. Panofsky, H.A. Vertical Variation of Roughness Length at the Boulder Atmospheric Observatory. *Bound. Layer Meteorol.* **1984**, *28*, 305–308. [[CrossRef](#)]
43. Businger, J.A.; Miyake, M.; Dyer, A.J.; Bradley, E.F. On the direct determination of the turbulent heat flux near the ground. *J. Appl. Meteorol.* **1967**, *6*, 1025–1032. [[CrossRef](#)]
44. Paulson, C.A. The mathematical representation of wind speed and temperature profiles in the unstable atmospheric surface layer. *J. Appl. Meteorol.* **1970**, *9*, 857–861. [[CrossRef](#)]
45. Brutsaert, W. *Evaporation into the Atmosphere: Theory, History and Applications*; Springer: Dordrecht, The Netherlands, 1982; p. 299.
46. Holzman, M.E.; Rivas, R.; Piccolo, M.C. Estimating soil moisture and the relationship with crop yield using surface temperature and vegetation index. *Int. J. Appl. Earth Obs. Geoinf.* **2014**, *28*, 181–192. [[CrossRef](#)]
47. Carlson, T.N.; Gillies, R.R.; Perry, E.M. A method to make use of thermal infrared temperature and NDVI measurements to infer surface soil water content and fractional vegetation cover. *Remote Sens. Rev.* **1994**, *9*, 161–173. [[CrossRef](#)]
48. Gillies, R.R.; Kustas, W.P.; Humes, K.S. A verification of the ‘triangle’ method for obtaining surface soil water content and energy fluxes from remote measurements of the Normalized Difference Vegetation Index (NDVI) and surface e. *Int. J. Remote Sens.* **1997**, *18*, 3145–3166. [[CrossRef](#)]
49. Patel, N.R.; Anapashsha, R.; Kumar, S.; Saha, S.K.; Dadhwal, V.K. Assessing potential of MODIS derived temperature/vegetation condition index (TVDI) to infer soil moisture status. *Int. J. Remote Sens.* **2009**, *30*, 23–39. [[CrossRef](#)]
50. Anderson, M.C.; Kustas, W.P.; Alfieri, J.G.; Gao, F.; Hain, C.; Prueger, J.H.; Evett, S.; Colaizzi, P.; Howell, T.; Chavez, J.L. Mapping daily evapotranspiration at Landsat spatial scales during the BEAREX’08 field campaign. *Adv. Water Resour.* **2012**, *50*, 162–177. [[CrossRef](#)]
51. Anderson, M.C.; Kustas, W.P.; Norman, J.M.; Hain, C.R.; Mecikalski, J.R.; Schultz, L.; Gonzalez-Dugo, M.P.; Cammalleri, C.; D’urso, G.; Pimstein, A.; et al. Mapping daily evapotranspiration at field to continental scales using geostationary and polar orbiting satellite imagery. *Hydrol. Earth Syst. Sci.* **2011**, *15*, 223–239. [[CrossRef](#)]
52. Anderson, M.C.; Norman, J.M.; Mecikalski, J.R.; Otkin, J.A.; Kustas, W.P. A climatological study of evapotranspiration and moisture stress across the continental United States based on thermal remote sensing: 2. Surface moisture climatology. *J. Geophys. Res. Atmos.* **2007**, *112*. [[CrossRef](#)]

53. Anderson, M.C.; Norman, J.M.; Mecikalski, J.R.; Otkin, J.A.; Kustas, W.P. A climatological study of evapotranspiration and moisture stress across the continental United States based on thermal remote sensing: 1. Model formulation. *J. Geophys. Res. Atmos.* **2007**, *112*. [[CrossRef](#)]
54. Norman, J.M.; Anderson, M.C.; Kustas, W.P.; French, A.N.; Mecikalski, J.; Torn, R.; Diak, G.R.; Schmugge, T.J.; Tanner, B.C.W. Remote sensing of surface energy fluxes at 10(1)-m pixel resolutions. *Water Resour. Res.* **2003**, *39*. [[CrossRef](#)]
55. Norman, J.M.; Kustas, W.P.; Humes, K.S. Source Approach for Estimating Soil and Vegetation Energy Fluxes in Observations of Directional Radiometric Surface-Temperature. *Agric. For. Meteorol.* **1995**, *77*, 263–293. [[CrossRef](#)]
56. Xia, T.; Kustas, W.P.; Anderson, M.C.; Alfieri, J.G.; Gao, F.; McKee, L.; Prueger, J.H.; Geli, H.M.E.; Neale, C.M.U.; Sanchez, L.; et al. Mapping evapotranspiration with high-resolution aircraft imagery over vineyards using one- and two-source modeling schemes. *Hydrol. Earth Syst. Sci.* **2016**, *20*, 1523–1545. [[CrossRef](#)]
57. Anderson, M.C.; Allen, R.G.; Morse, A.; Kustas, W.P. Use of Landsat thermal imagery in monitoring evapotranspiration and managing water resources. *Remote Sens. Environ.* **2012**, *122*, 50–65. [[CrossRef](#)]
58. Kustas, W.P.; Alfieri, J.G.; Anderson, M.C.; Colaizzi, P.D.; Prueger, J.H.; Evett, S.R.; Neale, C.M.U.; French, A.N.; Hipps, L.E.; Chavez, J.L.; et al. Evaluating the two-source energy balance model using local thermal and surface flux observations in a strongly advective irrigated agricultural area. *Adv. Water Resour.* **2012**, *50*, 120–133. [[CrossRef](#)]
59. Horst, T.W.; Weil, J.C. Footprint Estimation for Scalar Flux Measurements in the Atmospheric Surface-Layer. *Bound. Layer Meteorol.* **1992**, *59*, 279–296. [[CrossRef](#)]
60. Horst, T.W.; Weil, J.C. How Far Is Far Enough—The Fetch Requirements for Micrometeorological Measurement of Surface Fluxes. *J. Atmos. Ocean Technol.* **1994**, *11*, 1018–1025. [[CrossRef](#)]
61. Kustas, W.P.; Norman, J.M. A two-source energy balance approach using directional radiometric temperature observations for sparse canopy covered surfaces. *Agron. J.* **2000**, *92*, 847–854. [[CrossRef](#)]
62. Geli, H.M.E. Modeling Spatial Surface Energy Fluxes of Agricultural and Riparian Vegetation Using Remote Sensing. Ph.D. Thesis, Utah State University, Logan, UT, USA, 2012.
63. Prueger, J.H.; Hatfield, J.L.; Kustas, W.P.; Hipps, L.E.; MacPherson, J.I.; Neale, C.M.U.; Eichinger, W.E.; Cooper, D.I.; Parkin, T.B. Tower and aircraft eddy covariance measurements of water vapor, energy, and carbon dioxide fluxes during SMACEX. *J. Hydrometeorol.* **2005**, *6*, 954–960. [[CrossRef](#)]
64. Meek, D.W.; Prueger, J.H.; Kustas, W.P.; Hatfield, J.L. Determining meaningful differences for SMACEX eddy covariance measurements. *J. Hydrometeorol.* **2005**, *6*, 805–811. [[CrossRef](#)]
65. Evans, J.G.; McNeil, D.D.; Finch, J.W.; Murray, T.; Harding, R.J.; Ward, H.C.; Verhoef, A. Determination of turbulent heat fluxes using a large aperture scintillometer over undulating mixed agricultural terrain. *Agric. For. Meteorol.* **2012**, *166*, 221–233. [[CrossRef](#)]
66. Foken, T. The energy balance closure problem: An overview. *Ecol. Appl.* **2008**, *18*, 1351–1367. [[CrossRef](#)]
67. Hollinger, D.Y.; Richardson, A.D. Uncertainty in eddy covariance measurements and its application to physiological models. *Tree Physiol.* **2005**, *25*, 873–885. [[CrossRef](#)]
68. Schmidt, A.; Hanson, C.; Chan, W.S.; Law, B.E. Empirical assessment of uncertainties of meteorological parameters and turbulent fluxes in the AmeriFlux network. *J. Geophys. Res. Biogeosci.* **2012**, *117*. [[CrossRef](#)]
69. Liu, S.M.; Xu, Z.W.; Zhu, Z.L.; Jia, Z.Z.; Zhu, M.J. Measurements of evapotranspiration from eddy-covariance systems and large aperture scintillometers in the Hai River Basin, China. *J. Hydrol.* **2013**, *487*, 24–38. [[CrossRef](#)]
70. De Bruin, H.A.R.; Van Den Hurk, B.; Kroon, L.J.M. On the temperature-humidity correlation and similarity. *Bound. Layer Meteorol.* **1999**, *93*, 453–468. [[CrossRef](#)]
71. De Bruin, H.A.R.; Bink, N.J.; Kroon, L.J.M. Fluxes in the surface layer under advective conditions. In *Land Surface Evaporation*; Springer: Berlin/Heidelberg, Germany, 1991; pp. 157–169.
72. Monteith, J.L. *Principles of Environmental Physics*; Edward Arnold Press: London, UK, 1973; p. 241.
73. Priestley, C.H.B.; Taylor, R.J. On the Assessment of Surface Heat Flux and Evaporation Using Large-Scale Parameters. *Mon. Weather Rev.* **1972**, *100*, 81–92. [[CrossRef](#)]
74. Ezzahar, J.; Chehbouni, A.; Hoedjes, J.C.B.; Chehbouni, A. On the application of scintillometry over heterogeneous grids. *J. Hydrol.* **2007**, *334*, 493–501. [[CrossRef](#)]
75. Price, J.C. Using Spatial Context in Satellite Data to Infer Regional Scale Evapotranspiration. *IEEE Trans. Geosci. Remote Sens.* **1990**, *28*, 940–948. [[CrossRef](#)]

76. McVicar, T.R.; Jupp, D.L.B. The current and potential operational uses of remote sensing to aid decisions on drought exceptional circumstances in Australia: A review. *Agric. Syst.* **1998**, *57*, 399–468. [[CrossRef](#)]
77. Long, D.; Singh, V.P. Assessing the impact of end-member selection on the accuracy of satellite-based spatial variability models for actual evapotranspiration estimation. *Water Resour. Res.* **2013**, *49*, 2601–2618. [[CrossRef](#)]
78. Long, D.; Singh, V.P. A Two-Source Trapezoid Model for Evapotranspiration (TTME) from Satellite Imagery. *Remote Sens. Environ.* **2012**, *121*, 370–388. [[CrossRef](#)]
79. Hoedjes, J.C.B.; Zuurbier, R.M.; Watts, C.J. Large aperture scintillometer used over a homogeneous irrigated area, partly affected by regional advection. *Bound. Layer Meteorol.* **2002**, *105*, 99–117. [[CrossRef](#)]
80. Kustas, W.P.; Prueger, J.H.; Hipps, L.E.; Hatfield, J.L.; Meek, D. Inconsistencies in net radiation estimates from use of several models of instruments in a desert environment. *Agric. For. Meteorol.* **1998**, *90*, 257–263. [[CrossRef](#)]
81. Kohsiek, W.; Liebenthal, C.; Foken, T.; Vogt, R.; Oncley, S.P.; Bernhofer, C.; Debruin, H.A.R. The energy balance experiment EBEX-2000. Part III: Behaviour and quality of the radiation measurements. *Bound. Layer Meteorol.* **2007**, *123*, 55–75. [[CrossRef](#)]
82. Hemakumara, H.M.; Chandrapala, L.; Moene, A.F. Evapotranspiration fluxes over mixed vegetation areas measured from large aperture scintillometer. *Agric. Water Manag.* **2003**, *58*, 109–122. [[CrossRef](#)]



© 2019 by the authors. Licensee MDPI, Basel, Switzerland. This article is an open access article distributed under the terms and conditions of the Creative Commons Attribution (CC BY) license (<http://creativecommons.org/licenses/by/4.0/>).